A complex node of the cosmic web associated with the massive galaxy cluster MACS J0600.1-2008

Lukas J. Furtak [1]★ Adi Zitrin [1] Johan Richard [2] Dominique Eckert,[3] Jack Sayers [4]
Harald Ebeling [5] Seiji Fujimoto [6] Nicolas Laporte [7] David Lagattuta [8,9] Marceau Limousin,[7]
Guillaume Mahler [10] Ashish K. Meena [1] Felipe Andrade-Santos,[11,12] Brenda L. Frye,[13]
Mathilde Jauzac [8,9,14,15] Anton M. Koekemoer [16] Kotaro Kohno [17,18] Daniel Espada,[19,20] Harry Lu,[4]
Richard Massey [8,9] and Anna Niemiec [21]

Affiliations are listed at the end of the paper

ABSTRACT

MACS J0600.1-2008 (MACS0600) is an X-ray-luminous, massive galaxy cluster at $z_{\rm d} = 0.43$, studied previously by the *REionization LensIng Cluster Survey* and *ALMA Lensing Cluster Survey* projects which revealed a complex, bimodal mass distribution and an intriguing high-redshift object behind it. Here, we report on the results of a combined analysis of the extended strong lensing (SL), X-ray, Sunyaev–Zeldovich (SZ), and galaxy luminosity-density properties of this system. Using new *JWST* and ground-based *Gemini-N* and *Keck* data, we obtain 13 new spectroscopic redshifts of multiply-imaged galaxies and identify 12 new photometric multiple-image systems and candidates, including two multiply-imaged $z \sim 7$ objects. Taking advantage of the larger areal coverage, our analysis reveals an additional bimodal, massive SL structure which we measure spectroscopically to lie adjacent to the cluster and whose existence was implied by previous SL-modelling analyses. While based in part on photometric systems identified in ground-based imaging requiring further verification, our extended SL model suggests that the cluster may have the second-largest critical area and effective Einstein radius observed to date, $A_{\rm crit} \simeq 2.16 \, {\rm arcmin}^2$ and $\theta_{\rm E} = 49.7'' \pm 5.0''$ for a source at $z_{\rm s} = 2$, enclosing a total mass of $M(< \theta_{\rm E}) = (4.7 \pm 0.7) \times 10^{14} \, {\rm M}_\odot$. These results are also supported by the galaxy luminosity distribution, and the SZ and X-ray data. Yet another, probably related massive cluster structure, discovered in X-rays 5 arcmin (1.7 Mpc) further north, suggests that MACS0600 is part of an even larger filamentary structure. This discovery adds to several recent detections of massive structures around SL galaxy clusters and establishes MACS0600 as a prime target for future high-redshift surveys with *JWST*.

Key words: gravitational lensing: strong – galaxies: clusters: individual: MACS J0600.1-2008 – galaxies: clusters: intracluster medium – dark matter – large-scale structure of Universe – X-rays: galaxies: clusters.

1 INTRODUCTION

As the most massive gravitationally bound structures in the Universe, galaxy clusters form relatively late in cosmic history at the nodes of the cosmic web (e.g. Zeldovich, Einasto & Shandarin 1982; de Lapparent, Geller & Huchra 1986) where streams of matter fall into dense cluster cores (e.g. Klypin & Shandarin 1983; Diaferio & Geller 1997; Springel et al. 2005; Dubois et al. 2014; Ata et al. 2022). As a result, massive galaxy clusters are often not yet fully virialized when we observe them, exhibiting merging cores (e.g. Carrasco et al. 2010; Jauzac et al. 2014; Pascale et al. 2022a; Diego et al. 2023a, b), disturbed X-ray gas (e.g. Borgani & Guzzo 2001; Ebeling, Barrett & Donovan 2004; Merten et al. 2011), intra-cluster light (e.g. Durret et al. 2016; Ellien et al. 2019), radio relics (e.g. Bonafede et al. 2012; Finner et al. 2017, 2021), and extended massive structures far outside their cores (e.g. Kartaltepe et al. 2008; Jauzac

et al. 2012, 2018; Medezinski et al. 2016; Furtak et al. 2023a). In light of this complexity, gravitational lensing represents the method of choice to constrain the distribution of otherwise invisible dark matter (DM) in and around evolving galaxy clusters since lensing is sensitive to the projected mass density distribution yet does not rely on the assumption of hydrostatic equilibrium (e.g. Geller et al. 2013). In fact, multiple DM cores and substructure are known to often enhance and extend the strong-lensing (SL) regime (e.g. Meneghetti, Bartelmann & Moscardini 2003; Torri et al. 2004; Meneghetti et al. 2007a, b; Redlich et al. 2012; Zitrin et al. 2013a, b).

Massive and merging SL clusters that cover a relatively large area on the sky are particularly valuable as 'cosmic telescopes' that use the gravitational magnification of the cluster to enable the study of faint objects in the background which would otherwise not be observable (e.g. Maizy et al. 2010; Sharon et al. 2012; Monna et al. 2014; Coe, Bradley & Zitrin 2015; Coe et al. 2019). Indeed, due to the magnification provided by SL, cluster surveys conducted with the *Hubble Space Telescope* (*HST*) were able to detect several hundreds of high-redshift ($z \sim 6$–10) galaxies down

★ E-mail: furtak@post.bgu.ac.il

to luminosities of $M_{UV} \lesssim -13$ (e.g. Bouwens et al. 2017, 2022; Livermore, Finkelstein & Lotz 2017; Atek et al. 2018; Ishigaki et al. 2018) and stellar masses of $M_\star \gtrsim 10^6$ M$_\odot$ (e.g. Bhatawdekar et al. 2019; Kikuchihara et al. 2020; Strait et al. 2020, 2021; Furtak et al. 2021). More recently, cluster observations with *JWST* (Gardner et al. 2023; McElwain et al. 2023) discovered the first galaxy candidates at $z > 10$ (e.g. Adams et al. 2023; Atek et al. 2023a; Bradley et al. 2023), enabled the first rest-frame optical spectroscopy at $z > 6$ (e.g. Hsiao et al. 2023; Roberts-Borsani et al. 2023; Williams et al. 2023) which confirmed the high ionization power of low-mass galaxies in the early Universe (Atek et al. 2024a), and uncovered a new population of dust-obscured active galactic nuclei, the so-called 'little red dots' (Furtak et al. 2023b, 2024b; Labbe et al. 2023; Greene et al. 2024, see also Matthee et al. 2024). Due to the extreme magnifications achieved when a background object crosses the critical line, it has become possible to detect and study extremely compact star clusters and even single stars out to high redshifts (e.g. Kelly et al. 2018; Welch et al. 2022a, b; Meena et al. 2023; Furtak et al. 2024a). Finally, multiply-imaged supernovae (e.g. Frye et al. 2024) can be used to constrain cosmological parameters due to the delay in arrival time between the multiple images (e.g. Pascale et al. 2024). Discovering new, powerful cluster lenses is therefore a crucial step in preparation for the next generations of high-redshift surveys.

Although not yet virialized, massive merging clusters are usually well-defined overdensities in the cosmic web (e.g. Geller et al. 2014, 2016) and, at the same time, frequently connected to extended cosmic filaments, e.g. MACS J0717.5+3745 (e.g. Jauzac et al. 2012, 2018; Durret et al. 2016; Ellien et al. 2019) or Abell 2744 (Jauzac et al. 2016; Medezinski et al. 2016). The very existence of the most massive galaxy clusters such as e.g. *El Gordo* (e.g. Menanteau et al. 2012; Zitrin et al. 2013b; Molnar & Broadhurst 2015; Diego et al. 2023b; Frye et al. 2023), and even more so their observed number densities, have been claimed to pose a challenge to Lambda cold dark matter (ΛCDM) cosmology (e.g. Donahue et al. 1998; Mullis et al. 2005; Ebeling et al. 2007; Foley et al. 2011; Miller et al. 2018; Asencio, Banik & Kroupa 2021). Observing galaxy clusters at the high-mass end of the hierarchical Universe and constraining their total mass is crucial, since the extreme-value statistics of the cluster mass function constrain large-scale structure formation in the Universe (e.g. Frye et al. 2023) in the same way that the most massive galaxies constrain galaxy formation (e.g. Glazebrook et al. 2024).

In this work, we present the discovery of cluster-scale structures associated with the massive cluster lens MACS J0600.1-2008 (also known as RXC J0600.1-2007; MACS0600 hereafter; Ebeling, Edge & Henry 2001), which was targeted in the *REionization LensIng Cluster Survey* (RELICS; Coe et al. 2019) with *HST* and the *ALMA Lensing Cluster Survey* (ALCS; Fujimoto et al. 2023; Kohno et al. 2023) program with the *Atacama Large Millimeter/submillimeter Array* (ALMA). The cluster was previously known for hosting a Type Ia supernova (Coe et al. 2019; Golubchik et al. 2023) and the quintuple image of an ALMA-detected galaxy at $z = 6.0719 \pm 0.0004$ (Fujimoto et al. 2021; Laporte et al. 2021), which we recently observed at high resolution with *JWST* (Fujimoto et al. 2024). We derive an improved SL model for MACS0600 based on new observations and, for the first time, model the extended mass distribution of the cluster.

This paper is organized as follows: In Section 2 we present the data sets used in this work. Section 3 describes our SL analysis methods. The results are then presented in Section 4 and discussed in Section 5. Finally, we conclude this paper in Section 6. Throughout this work, we assume a standard flat ΛCDM cosmology with $H_0 = 70$ km s^{-1} Mpc^{-1}, $\Omega_\Lambda = 0.7$, and $\Omega_m = 0.3$. All magnitudes are quoted in the AB system (Oke & Gunn 1983), and all quoted uncertainties represent 1σ confidence limits unless stated otherwise.

2 TARGET AND OBSERVATIONS

This study focuses on galaxy cluster structures detected northeastwards of the X-ray-luminous galaxy cluster MACS0600 (Ebeling et al. 2001), just beyond the field of view of the *HST* observations taken in the framework of the RELICS program. Note that MACS0600 was selected for RELICS precisely because of its high Sunyaev–Zeldovich (SZ; Sunyaev & Zeldovich 1972) mass (Coe et al. 2019) of $M_{500,SZ} = 10.73^{+0.51}_{-0.54} \times 10^{14}$ M$_\odot$ (Planck Collaboration XXVII 2016).

A significant mass outside of the cluster was first suspected due to difficulties in reproducing the strongly lensed multiple images in MACS0600. We therefore obtained optical imaging with the *Gemini-North* telescope (*Gemini-N*) and indeed find a prominent overdensity of cluster galaxies north-east of the RELICS field of view (see Fig. 1). Initial estimates, based on galaxy velocity dispersions (see Section 4.1), suggest that this structure might even be more massive than the *HST*-observed part of MACS0600. We therefore dub this cluster the 'Anglerfish cluster', since analogous to the deep-sea creature we have been observing only part of it all this time, thereby missing the other, perhaps larger part. From here on, we will refer to the new structure in the north-east as the 'eastern' part of the cluster, the southern part of MACS0600 (formerly its centre) as the 'southern' structure, and the structure north of it as the 'western' clump, as shown in Fig. 1.

The following sections describe the observations used in this study: our *Gemini-N* observations in Section 2.1, recent *JWST* imaging of the southern clump in Section 2.2, the RELICS data set in Section 2.3, and additional ancillary spectroscopy, ground-based imaging, X-ray, and submillimetre observations in Sections 2.5 and 2.6. The relative positions and coverages of the various data sets used here are shown in Fig. 2 and an overview of the observations is given in Table 1.

2.1 *Gemini-N*/GMOS observations

To observe the structures suspected outside of the RELICS field of view of MACS0600 (the 'eastern' part of the cluster), we obtained broad-band imaging data with the *Gemini Multi-Object Spectrograph* (GMOS; Hook et al. 2004) on *Gemini-N* in three filters: g, r, and i (Program ID: GN-2020B-Q-903; PI: A. Zitrin). The observations of the region north-east of MACS0600 total 40 min integration time per band. The data are first reduced and co-added with the standard GMOS pipeline in the DRAGONS package (v3.0.1; Labrie et al. 2021), background-subtracted with PHOTUTILS (v1.4.0; Bradley et al. 2022), and then registered to the astrometry of the *Wide-field Infrared Survey Explorer* point-source catalogue (Wright et al. 2010) using SCAMP (Bertin 2006). This last step ensures that we are using the same astrometry as the existing RELICS catalogue (Coe et al. 2019, see Section 2.3). The final images achieve a pixel scale of 0.16 arcsec pix^{-1}. We run SEXTRACTOR (Bertin & Arnouts 1996) in dual-image mode, with a stack of the three GMOS bands as the detection image, to detect sources and measure photometry. The photometry is then corrected for galactic extinction using the Schlafly & Finkbeiner (2011) dust emission maps.

Within the same program, we also obtained 2.3 h of *Gemini-N*/GMOS slit-spectroscopy of selected objects both within the MACS0600 *HST* field of view and the region in the new eastern part. We in particular targeted the suspected brightest cluster galaxies (BCGs) of the cluster structure in the east. The data were reduced
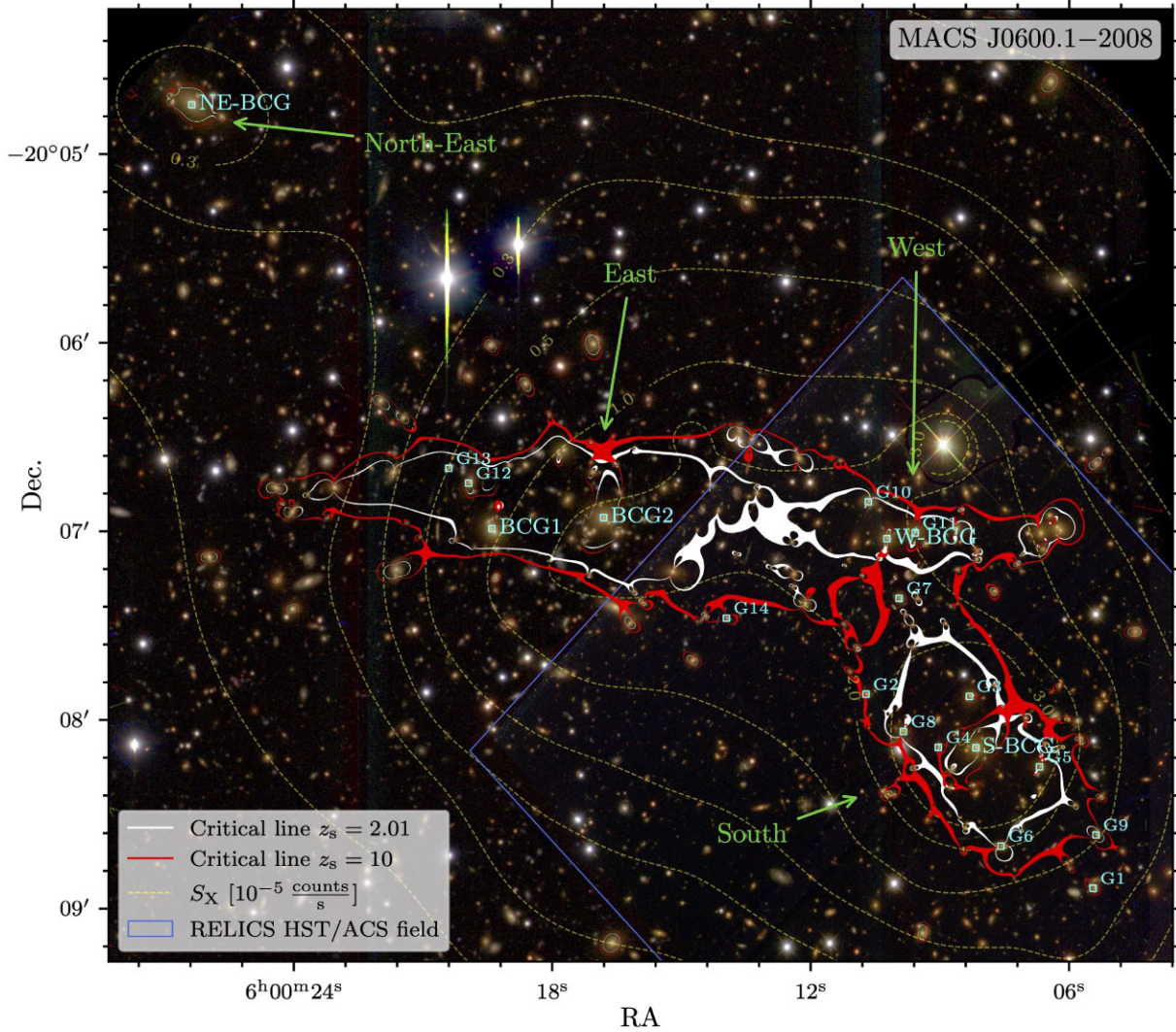
Figure 1. Combined *HST*/ACS and *Gemini-N*/GMOS composite-colour image (blue: *g* + *F*435*W*, green: *r* + *F*606*W*, red: *i* + *F*814*W*) of MACS0600. The BCGs of the cluster (Section 3.1) and a number of cluster member galaxies of interest (see Table 2) are shown in cyan. Overlaid are the critical curves of our SL model (Section 4.3) for $z_s = 2.01$ (corresponding to system 1) and $z_s = 10$ in white and red, respectively. The green arrows designate the various cluster substructures analysed in this work. The X-ray surface brightness (see Sections 2.6 and 4.2, and Fig. 6) is overlaid as yellow contours in steps of $[0.1, 0.2, 0.3, 0.5, 1.0, 2.0, 3.0] \times 10^{-5}$ counts s^{-1}. The RELICS *HST*/ACS field of view (Section 2.3) is shown in blue. We nickname MACS0600 'Anglerfish cluster' analogous to the deep-sea creature of which often only one part is immediately seen and the bulk remains hidden. A full-resolution (0.06 arcsec pix^{-1}), fully vectorized version of this figure is included in the online supplementary material of this paper.

and spectra extracted using the *Gemini*IRAF data reduction package.[1] The data reduction workflow includes bias subtraction, flat-fielding, and wavelength calibration using a CUAR lamp illuminating our mask. Flux calibration was performed using the white dwarf Wolf 1346 as a standard star. The final spectra achieve 1σ-sensitivities of 9×10^{-19} erg s^{-1} cm^{-2} Å^{-1}.

2.2 *JWST* imaging

MACS0600 has also recently been observed with *JWST* in cycle 1 (Program ID: GO-1567; PI: S. Fujimoto), both with the *Near Infrared Camera* (NIRCam; Rieke et al. 2023) and the *Near Infrared Spectrograph* (NIRSpec; Jakobsen et al. 2022; Böker et al. 2023) integral field unit (Böker et al. 2022) targeted at the ALMA-detected

[1]https://www.gemini.edu/observing/phase-iii/reducing-data

$z = 6.07$ arc (Fujimoto et al. 2021; Laporte et al. 2021). The *JWST* observations and results are published in Fujimoto et al. (2024).

For the purpose of this work, we use the NIRCam imaging, which comprises five broad-band filters: *F*115*W*, *F*150*W*, *F*277*W*, *F*356*W*, and *F*444*W*. The images have exposure times of 30 min in *F*115*W* and *F*277*W*, 1.4 h in *F*150*W*, and 40 min in *F*356*W* and *F*444*W*. After initial calibration with the *JWST* calibration pipeline (Bushouse et al. 2024), the data, retrieved from the Mikulski Archive for Space Telescopes (MAST), were reduced and drizzled into mosaics with the grism redshift and line analysis software for space-based spectroscopy pipeline (grizli; Brammer 2023). The final short-wavelength (SW; i.e. *F*115*W* and *F*150*W*) mosaics have resolutions of 0.02 arcsec per pixel and the long-wavelength (LW; *F*277*W*, *F*356*W*, and *F*444*W*) mosaics of 0.04 arcsec per pixel. The footprint of the *JWST* imaging compared to the other available data sets can be seen in Fig. 2. We refer the
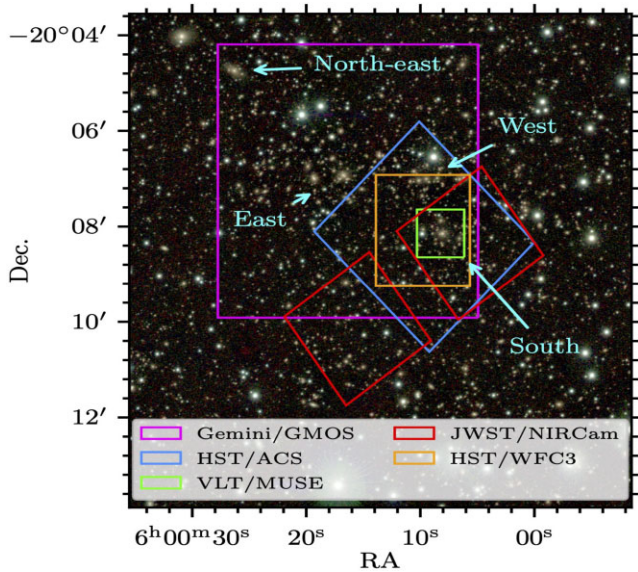
Figure 2. Cut-out of a VIRCAM colour-composite image (blue: *Y* band, green: *J* band, red: *Ks* band) overlaid with the field of views of the various observations of the MACS0600 used in this work (see Sections 2.1, 2.2, 2.3, 2.4, and 2.6).

Table 1. Summary of observations used in this work. The pointings of the most important data sets can be seen in Fig. 2.

Instrument	Exposure time	Reference
Imaging		
Gemini-N/GMOS	40 min	This work
JWST/NIRCam	0.5–1.5 h	Fujimoto et al. (2024)
HST/ACS & WFC3	0.5–1 orbits	RELICS; Coe et al. (2019)
VISTA/VIRCAM	45 min	GCAV
UH 2.2 m telescope	240 s	Repp & Ebeling (2018)
Spectroscopy		
Gemini-N/GMOS	2.3 h	This work
VLT/MUSE	7.3 h	This work
Keck/DEIMOS	1.0 h	This work
Ancillary		
XMM–Newton	42 ks	CHEX-MATE
ACT	–	Mallaby-Kay et al. (2021)

reader to Fujimoto et al. (2024) for more details on the reduction and processing of the NIRCam images.

2.3 Archival RELICS *HST* imaging data

In addition, we have at our disposal the public data set of the RELICS program. The RELICS *HST* imaging data of MACS0600 comprise mosaics in seven broad-band filters of the *Advanced Camera for Survey* (ACS) and the *Wide Field Camera Three* (WFC3): *F*435*W*, *F*606*W*, *F*814*W*, *F*105*W*, *F*125*W*, *F*140*W*, and *F*160*W*, which are available in the RELICS repository on the `Mikulski Archive for Space Telescopes` (MAST). In this work we use the ACS + WFC3 catalogue, also available in MAST, which contains *HST* fluxes obtained with `SEXTRACTOR` and photometric redshifts computed with the `Bayesian Photometric Redshifts` code (BPZ; Benítez 2000; Coe et al. 2006). We refer the reader to Coe et al.

(2019) for the details of data reduction, catalogue assembly, and photometric redshift computation.

2.4 VLT/MUSE spectroscopy

Spectroscopic observations of the southern clump of MACS0600 were performed with the ESO *Very Large Telescope* (VLT) *Multi Unit Spectroscopic Explorer* (MUSE; Bacon et al. 2010) (Program ID: 0100.A-0792(A); PI: A. Edge, and Program ID: 109.22VV.001(A); PI: S. Fujimoto), in 2018 January and 2022 September–December, respectively. The 2018 observations were taken without adaptive optics, during three exposures of 900 s each and are thus relatively shallow. The 2022 observations use the adaptive optics system (WFM-AO-N) and comprise of 18 exposures of 1284 s each. The MUSE pointing was centred on α =06:00:08.8 and δ =-20:08:08 in both cases (see Fig. 2).

We follow the procedure described in Richard et al. (2021) for all steps related to the data reduction, spectral extraction, and redshift measurements. This approach is optimized for deep MUSE observations towards crowded lensing cluster fields. The basic steps of data reduction use version `v2.7` of the ESO data reduction software (Weilbacher et al. 2020) (which includes correction to the heliocentric frame), but include the self-calibration and sky subtraction steps with a specifically adjusted object mask to account for the extended light envelopes of cluster member galaxies. Individual exposures are resampled on to the same cube sampling grid and then the cubes are combined with the `MPDAF` (Piqueras et al. 2019) cube combination recipes.[2] Higher systematics in sky background are removed by masking specific inter-stack regions of the MUSE slicer in individual cubes. The combined cube is then processed with the `ZAP` (v2; Soto et al. 2016) software which performs additional subtraction of sky residuals with a principle component analysis technique. Finally, absolute astrometry of the combined data cube is calibrated against available *HST* images. Image quality is measured in the final data cube to be 0.59 arcsec full width at half-maximum (FWHM) at 7000 Å.

Following Richard et al. (2021), source detection is performed using a combination of *HST*-based priors (from the RELICS *HST* catalogue; see Section 2.3) and a full search for line emitters in the MUSE cube using the `MUSELET` software.[3] MUSE spectra are extracted using the optimized algorithm from Horne (1986), and include a subtraction of the local background. The spectra are then run through the `MARZ` software (Hinton et al. 2016) to identify possible redshift solutions through cross-correlation with spectral templates. These solutions are finally inspected and each source is assessed a final redshift and a confidence level ranging from 1 to 3, where 3 is the most reliable.

2.5 *Keck*/DEIMOS spectroscopy

Additional multi-object spectroscopy (MOS) observations of MACS0600 were performed on 2016 October 28, with the *DEep Imaging Multi-Object Spectrograph* (DEIMOS; Faber et al. 2003) on the *Keck-2* 10 m telescope on Maunakea, Hawaii. The individual MOS targets were selected from prior wide-field imaging observations of the system conducted with the University of Hawaii (UH) 2.2 m telescope in the *V*-, *R*-, and *I*-band filters, using the resulting colour information of galaxies in the target field as an indicator of

---

[2]https://mpdaf.readthedocs.io/en/latest/cubelist.html
[3]https://mpdaf.readthedocs.io/en/latest/muselet.html

likely cluster membership (Repp & Ebeling 2018). The spectra were taken in three exposures of 1200 s each. Since only a single mask was designed and observed, priority was given to maximizing the number of target galaxies of a common colour without attempting to achieve statistical completeness either in magnitude or colour space. Using a 1 arcsec slit width and a central wavelength of 6300 Å, the instrumental set-up for the DEIMOS follow-up observations combined the 600 line mm^{-1} Zerodur grating with a GG455 order-blocking filter, resulting in a 1.2 Å per pixel sampling. We measured redshifts by cross-correlation with spectral templates and applied corrections to the heliocentric frame using an adaptation of the SPECPRO package (Masters & Capak 2011).

2.6 Ancillary data

Additional ancillary data available for MACS0600 include wide-field near-infrared (NIR) imaging taken with the *VISTA infrared camera* (VIRCAM; Dalton et al. 2006) on ESO's *Visible and Infrared Survey Telescope for Astronomy* (VISTA) in the framework of the *Galaxy Clusters At VIRCAM* survey (GCAV; Program ID: 198.A-2008(E); PI: M. Nonino). The reduced *Y*-, *J*-, and *Ks*-band images achieve 5σ depths of 23.5 mag and their 1.5 × 1.2 deg field of view is optimal for detecting possible extended structures around the cluster. Initial studies of the extended cluster structures of MACS0600 were conducted using optical imaging from the UH 2.2 m telescope in the *V*, *R*, and *I* bands to depths of 240 s each.

We also reduced and analysed publicly available X-ray observations of MACS0600, obtained with *XMM–Newton* in the framework of the *Cluster HEritage project with XMM–Newton—Mass Assembly and Thermodynamics at the Endpoint of structure formation* (CHEX-MATE; CHEX-MATE Collaboration 2021) program, to study the distribution of the hot intra-cluster medium (ICM) gas and the large-scale environment of the system. MACS0600 was observed by *XMM–Newton* on two occasions (observation IDs: 0 650 381 401 and 0827050601) for a total exposure time of 42 ks. We reduced the two observations using XMMSASv20.0 and the X-COP analysis pipeline (Eckert et al. 2017; Ghirardini et al. 2019). We used the standard data reduction chains to extract clean event lists for the three *European Photon Imaging Camera* (Strüder et al. 2001; Turner et al. 2001) detectors (MOS1, MOS2, and PN), and constructed the light curve of the observation to filter-out time periods affected by soft proton flares. After flare filtering, the total clean observing time is of 30.2 ks for the two MOS detectors and 23.5 ks for the PN detector. We extract photon maps from each observation and each detector in five energy bands spanning the 0.5–7 keV band, and stacked the maps to increase their depth. The non-X-ray background was modelled using a large collection of filter-wheel-closed observations and rescaled to each observation by matching the high-energy count rates measured in the unexposed corners of the detectors. For more details on the procedure, we refer the reader to Ghirardini et al. (2019).

Last, we also use mm-wave data used to map the SZ effect of the cluster, using *Atacama Cosmology Telescope* (ACT) 90 and 150 GHz maps from ACT data release 5 (Mallaby-Kay et al. 2021), combined with *Planck* data (Naess et al. 2020). The angular resolution of the maps is set by the ACT PSF, which has an approximate FWHM of 2.1 and 1.4 arcmin at 90 and 150 GHz (Choi et al. 2020). To remove primary cosmic microwave background (CMB) anisotropies from the maps, we subtract the component-separated CMB map obtained from the COMMANDER algorithm in *Planck* data release 3 (Planck Collaboration IV 2020). Finally, note that MACS0600 was also observed in ALMA band 6 (1.1 mm) in the framework of the ALCS program, though we do not use these data in this study.

3 GRAVITATIONAL LENSING MASS MODELLING

We model the cluster using the new implementation of the parametric SL mass modelling code by Zitrin et al. (2015), which was presented in Pascale et al. (2022b) and Furtak et al. (2023a), often referred to as Zitrin-analytic in recent works. Similarly to other parametric codes (e.g. Jullo et al. 2007; Oguri 2010), it models the various components with typical parametric functions. For the smooth cluster DM components we use here a pseudo-isothermal elliptical mass distribution (PIEMD; e.g. Kassiola & Kovner 1993; Keeton 2001; Monna et al. 2017):

$$\Sigma(\xi) = \frac{\sigma_v^2}{2G}\left(r_{\mathrm{core}}^2 + \xi^2\right)^{-\frac{1}{2}}, \tag{1}$$

and cluster member galaxies are modelled as dual pseudo-isothermal ellipsoids (dPIEs; e.g. Kassiola & Kovner 1993; Keeton 2001; Elíasdóttir et al. 2007; Monna et al. 2017):

$$\Sigma(\xi) = \frac{\sigma_v^2 r_{\mathrm{cut}}^2}{2G\xi\left(r_{\mathrm{cut}}^2 - r_{\mathrm{core}}^2\right)}\left[\left(1 + \frac{r_{\mathrm{core}}^2}{\xi^2}\right)^{-\frac{1}{2}} - \left(1 + \frac{r_{\mathrm{cut}}^2}{\xi^2}\right)^{-\frac{1}{2}}\right]. \tag{2}$$

In both equations, σ_v is the velocity dispersion of the profile, r_{core} and r_{cut} are core and truncation radii, respectively, and ξ is an elliptical coordinate defined as

$$\xi^2 = \frac{x^2}{(1-\epsilon)^2} + \frac{y^2}{(1+\epsilon)^2}. \tag{3}$$

The ellipticity ϵ is defined as

$$\epsilon = \frac{b-a}{a+b}, \tag{4}$$

where a and b are the semimajor and semiminor axes, respectively. Note that, in practice, the mass profiles (1) and (2) are implemented following the parametrization of Keeton (2001) and Oguri et al. (2010). We refer the reader to Furtak et al. (2023a) for more details on the method.

The cluster member galaxy selection is described in Section 3.1, the multiple images used to constrain the SL model of MACS0600 are described in Section 3.2, and finally the SL modelling set-up is described in Section 3.3.

3.1 Cluster member galaxies

Due to the fortunate availability of multiple data sets for this cluster, we use several methods to assemble a catalogue of cluster members in a hierarchical way.

First, we include all galaxies that have spectroscopic redshifts at the cluster redshift from the MUSE sample of MACS0600 (Fujimoto et al. 2021; Laporte et al. 2021) and the DEIMOS observations which extend further out into the eastern part of the cluster (see Section 2.5). The DEIMOS cluster members were selected based on their colours in the UH 2.2 m telescope imaging and we refer the reader to Fujimoto et al. (2021) for the MUSE spectroscopic cluster member selection. The combined samples contain 67 spectroscopic cluster members. The distribution of spectroscopic redshifts of the cluster member galaxies and the cluster redshift $z_d = 0.432$ (see below) are shown in Fig. 3. While the redshift distribution shown in Fig. 3 hints that there may be two distinct overdensities of galaxies at slightly different redshifts, we find the DEIMOS cluster members with $\langle z \rangle = 0.445$ to be uniformly distributed across the field. This rather suggests that MACS0600 is a large single cluster with some elongation along the line of sight. We also note that the spectroscopic redshifts of the
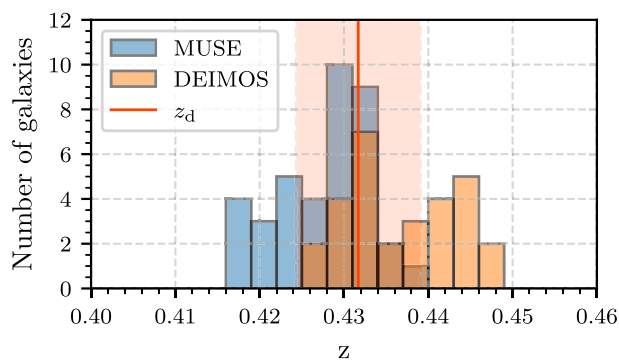
Figure 3. Spectroscopic redshift distribution of galaxies in MACS0600. The blue histogram represents the MUSE spectroscopic cluster members in MACS0600 and the orange histogram shows spectroscopic redshifts obtained with DEIMOS which extend to the eastern substructure. The cluster redshift $z_d = 0.432 \pm 0.007$ is shown in red.
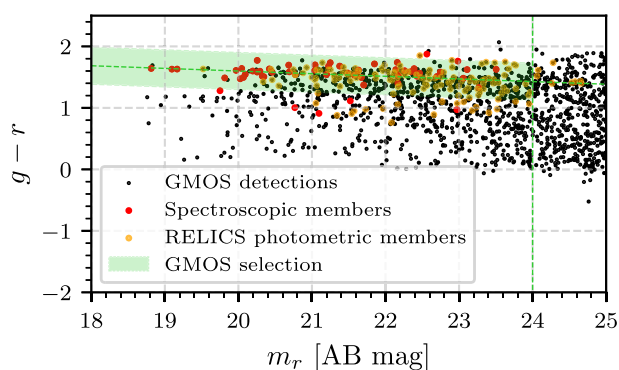
Figure 4. Colour–magnitude diagram of *Gemini-N*/GMOS sources (black dots). The red sequence is clearly visible in the $g - r$ colour which straddles the 4000 Å-break at the cluster redshift $z_d = 0.432$. We show the GMOS colours of known spectroscopic cluster members in red and of *HST* photometry-based cluster members in orange. Our GMOS red sequence selection window is shown in green.

cluster members slightly depart from the cluster redshift of $z_d = 0.46$ as reported from the MACS sample in Ebeling et al. (2001). This redshift was solely based on ground-based imaging and spectroscopy of the suspected BCG and therefore relatively uncertain. Averaging over all spectroscopically confirmed cluster members, we find an updated cluster redshift of $z_d = 0.432 \pm 0.007$ which we will use throughout the rest of this study.

Next, we complement this spectroscopic sample with cluster members photometrically selected as lying in the cluster's red sequence in a colour–magnitude analysis (e.g. Repp & Ebeling 2018). We first include the cluster member catalogue selected by the red sequence in the RELICS *HST* catalogues of MACS0600 which was already used in the previous SL models of the cluster (Fujimoto et al. 2021; Laporte et al. 2021). These cluster members, along with the spectroscopically selected ones, are then cross-matched with our GMOS catalogues, which enables us to calibrate the cluster's red sequence in $g - r$ colour space. We then select galaxies with r-band magnitudes $m_r < 24$ and within $g - r = \pm 0.3$ of the thus defined red sequence as shown in Fig. 4.

Combining these different selections, we obtain a catalogue totalling 504 cluster member galaxies across the *Gemini-N* and *HST* fields of view, 67 of which have spectroscopic redshifts. A table of cluster members is available in the online supplementary material

of this paper. The new cluster member sample confirms that the eastern structure of the cluster has two BCGs separated by 0.61 arcmin (0.21 Mpc). The RELICS BCG of MACS0600, which we will denominate 'South BCG' in accordance with the nomenclature adopted in Section 2, is separated by 2.88 arcmin (0.97 Mpc) from the cluster's BCG (BCG1). The brightest galaxy in the western clump (West BCG) is separated by 2.15 arcmin (0.72 Mpc) from BCG1 and by 1.21 arcmin (0.41 Mpc) from the South BCG. Interestingly, there is an extremely bright galaxy, the second brightest of our whole sample, in the north-eastern corner of the GMOS field of view (about 2.8 arcsec or 0.9 Mpc from BCG1) which also seems to present an overdensity of cluster members around it (see Fig. 1), suggesting an additional sub-clump in the north-east. Since we do not have any SL constraints close to that area (see Section 3.2 and Fig. 5), our SL model will not be able to well constrain its mass distribution. The cluster galaxy distribution does however suggest there to be even more extended structures to the cluster than visible in the GMOS imaging though, which we will discuss further in Section 5.2. The positions of these BCGs are shown in Fig. 1 and their properties summarized in Table 2.

3.2 Multiple image systems

The southern and western clumps of MACS0600 were already studied with the RELICS *HST* data (see Section 2.3) in Laporte et al. (2021) and Fujimoto et al. (2021) which yielded 10 multiple image systems, seven of which had spectroscopic redshifts either from the shallow MUSE data available at the time (see Section 3.2) and from GMOS and ALMA (Fujimoto et al. 2021; Laporte et al. 2021). Now, due to the *JWST*/NIRCam imaging (see Section 2.2), we are able to identify 17 additional multiple image systems and one candidate system in the southern clump, 13 of which lie within the new deep MUSE pointing (Fig. 2; see Section 2.4) and thus also have spectroscopic redshifts. Note that we only use spectroscopic redshifts with confidence levels ≥ 2. Unfortunately, the depth and spatial resolution of the *Gemini*/GMOS imaging (Section 2.1) are not high enough to securely identify multiple image candidates in the eastern part of the cluster. We nevertheless tentatively find two multiple image systems there, which are tentatively supported by our SL model (see Section 4.3), and two candidate systems.

All multiple images and candidates are shown in Fig. 5 and listed in detail in Table A1 in Appendix A. In total, we have identified 91 multiple images and candidates, belonging to 35 sources over the whole cluster field shown in Fig. 1. Systems 1 to 10 were used in the previous SL models of the cluster and system 7 is the $z = 6.0719 \pm 0.0004$ ALMA-detected system (Fujimoto et al. 2021; Laporte et al. 2021), quintuply imaged in a hyperbolic-umbilic-like configuration (Limousin et al. 2008; Meena & Bagla 2020; Lagattuta et al. 2023; Meena & Bagla 2023). The NIRCam imaging now confirms the fifth image of system 7 (image 7.5; Fujimoto et al. 2024) and one of the new NIRCam-identified systems, system 26, is a quadruply imaged galaxy–galaxy system. Systems 27 and 30 are clearly detected in the NIRCam data but appear neither in the *HST* nor the MUSE observation and are predicted at high redshift ($z > 6$) by our SL model (see Section 4.3). In the eastern part of the cluster, our SL model tentatively confirms (i.e. is able to reproduce) system candidates c24 and c33 but not the other candidates found in the GMOS imaging by eye. Finally, system candidates c31 and c32 are identified in the *HST* imaging, close to its eastern edge (see Fig. 2). We therefore also use them to constrain the newly discovered eastern structures of the cluster due to lack of constraints in that area, even
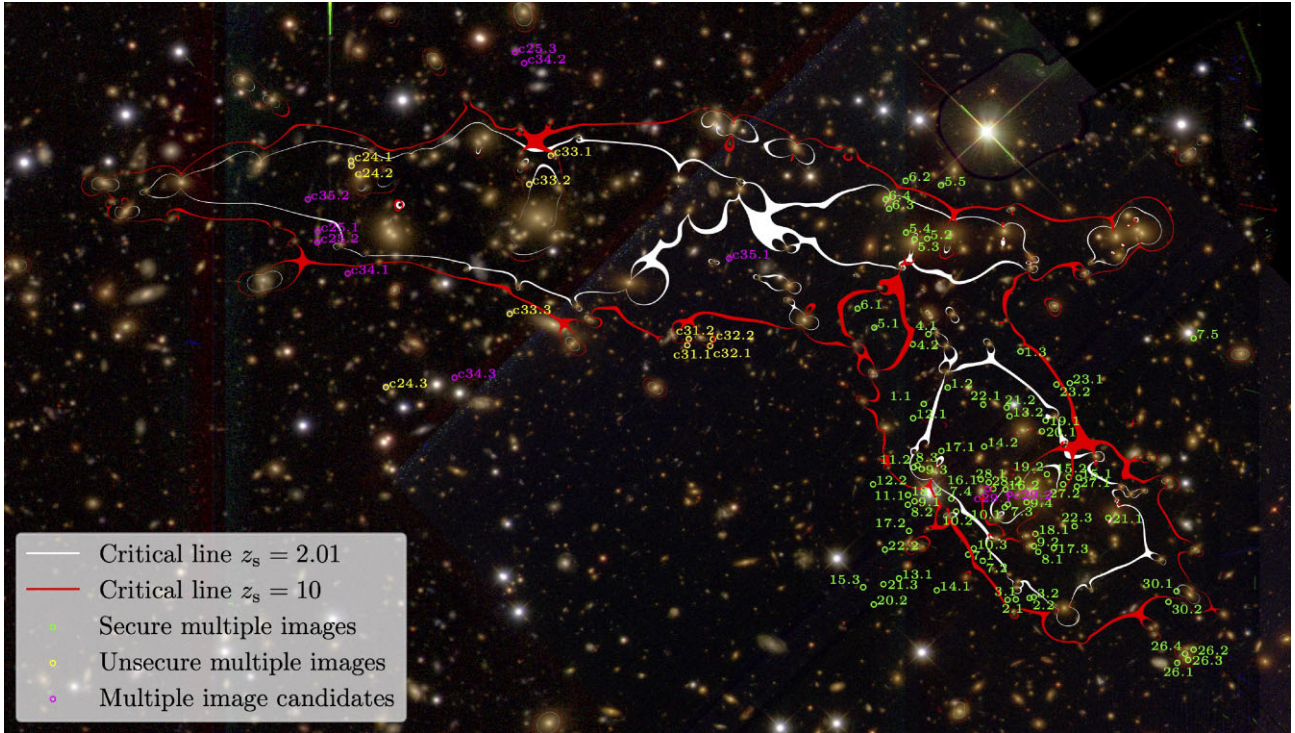
Figure 5. Combined ACS + GMOS composite colour image of MACS0600 as in Fig. 1, zoomed-in on the critical area of the cluster core. The critical lines of our SL model for sources at $z_s = 2.01$ (corresponding to system 1) and $z_s = 10$ are overlaid in white and red, respectively. The positions of multiple images are also noted (see also Table A1). The *green* images are spectroscopically confirmed images or other photometric images that are considered secure and are used as constraints in the modelling. Images labelled with 'c' are candidate systems mostly based on ground-based lower resolution imaging (see Section 2.1). Candidate images in *magenta* were not used in the modelling but the *yellow* ones were incorporated to anchor the eastern part of the cluster to the more reasonable-looking system candidates in that region. A full-resolution (0.06 arcsec pix^{-1}), fully vectorized version of this figure is included in the online supplementary material of this paper.

though they are less secure. Note that other candidate images, also marked 'c' in Table A1, are not used as constraints in the SL model.

3.3 Model set-up

Since the *HST*-part of MACS0600 was previously known from RELICS and modelled in Fujimoto et al. (2021) and Laporte et al. (2021), we follow these models and place two smooth PIEMD (1) DM haloes, one centred on the south BCG and one centred on the western BCG (see Table 2 and Fig. 1), and fix their centre positions. The extended eastern structure discovered in the GMOS imaging clearly presents two BCGs (Fig. 1), which often hints at there being two cluster-scale DM haloes. We therefore place two haloes in the main body, initially centred on BCG1 and BCG2. Preliminary SL models prefer the eastern-most halo to be centred north of its BCG. Its centre coordinates are therefore left as free parameters, whereas the other halo is fixed to be centred on BCG2.

The 504 cluster member galaxies identified in Section 3.1 are included in the model as dPIE (2) profiles. In order to reduce the otherwise gigantic number of free parameters, the cluster member dPIE parameters are scaled to a reference galaxy using luminosity scaling relations:

$$\sigma_v = \sigma_{v,\star} \left(\frac{L}{L_\star}\right)^\lambda, \tag{5}$$

$$r_{\text{core}} = r_{\text{core},\star} \left(\frac{L}{L_\star}\right)^\beta, \tag{6}$$

$$r_{\text{cut}} = r_{\text{cut},\star} \left(\frac{L}{L_\star}\right)^\alpha, \tag{7}$$

which is a common approach in parametric SL modelling (e.g. Halkola, Seitz & Pannella 2006, 2007; Jullo et al. 2007; Monna et al. 2014, 2015). We refer the reader to Furtak et al. (2023a) for more details on the implementation of this method in our code. In our model of MACS0600, we fix the core radius of the reference galaxy to $r_{\text{core},\star} = 0.2$ kpc and leave its velocity dispersion $\sigma_{v,\star}$ and truncation radius $r_{\text{cut},\star}$ as free parameters. The reference galaxy luminosity $L_\star$ corresponds to an absolute magnitude of $M = -21.04$ (in the *r* band), which was measured as the Schechter (Schechter 1976) exponential cut-off luminosity of our cluster member sample. The exponents in equations (5) to (7) are also free parameters in our model. Finally, it is possible to leave the relative weight of selected galaxies as free parameters if necessary, which we do for 16 cluster galaxies that lie close to multiple images used as constraints (see Table 2). The model does not include an external shear component (cf. Section 5.2).

The model is constrained by a total of 83 multiple images, belonging to 31 sources, 20 of which have spectroscopic redshifts (see Table A1). We assume a positional uncertainty of $\sigma_i = 0.5$ arcsec for each image and give a higher weight to system 7, the $z = 6.07$ quintuply-imaged system, by assigning it $\sigma_i = 0.25''$. Spectroscopic multiple image systems have fixed redshifts in the model and the redshifts of photometric systems are left as free parameters. As can be seen in Table A1, systems 4, 5, 6, 26, and 28 have relatively well-constrained photometric redshifts. We therefore also leave their redshifts as free parameters in the model but limit them to lie within the 95 per cent range of the photometric redshift. All other redshifts are left free to vary between $z = 0.8$ and $z = 6$ in the GMOS field of view and up to $z = 10$ in the *HST* and *JWST* fields of view (see Fig. 2). We do not use any parity information in this model.

Table 2. BCGs in MACS0600 cluster shown in Fig. 1 and other individual galaxies whose weight was left as a free parameter in our SL model (see Section 3.3).

Galaxy ID	RA[a]	Dec.[a]	m_r[a]	z_{spec}	σ_v[b] $\left[\frac{km}{s}\right]$	r_{core}[b] [kpc]	r_{cut}[b] [kpc]	M_{tot} [$10^{12}\,M_\odot$]
			BCGs shown in Fig. 1					
BCG1	06:00:19.40	−20:06:59.18	18.814 ± 0.013	0.4403 ± 0.0001	490^{+16}_{-21}	$0.375^{+0.006}_{-0.006}$	155^{+21}_{-26}	27^{+8}_{-9}
BCG2	06:00:16.81	−20:06:55.67	19.096 ± 0.013	0.4357 ± 0.0002	427^{+14}_{-19}	$0.335^{-0.005}_{-0.005}$	131^{+18}_{-22}	17^{+5}_{-6}
South BCG[c]	06:00:08.17	−20:08:08.85	19.913 ± 0.002	0.4266 ± 0.0002	406^{+14}_{-18}	$0.237^{+0.007\ d}_{-0.005}$	123^{+18}_{-20}	15^{+4}_{-5}
West BCG[c]	06:00:10.23	−20:07:02.37	20.018 ± 0.003	0.4460 ± 0.0002	341^{+38}_{-85}	$0.057^{+0.006\ d}_{-0.016}$	100^{+18}_{-34}	8^{+4}_{-7}
North-East BCG	06:00:26.37	−20:04:44.30	18.831 ± 0.013	–	477^{+16}_{-21}	$0.367^{+0.006}_{-0.005}$	150^{+20}_{-25}	25^{+7}_{-8}
			Cluster galaxies with a free weight (see Fig. 1)					
G1	06:00:05.45	−20:08:53.53	21.499 ± 0.008	–	183^{+12}_{-9}	$0.165^{+0.004}_{-0.008}$	47^{+7}_{-8}	$1.15^{+0.38}_{-0.40}$
G2	06:00:10.72	−20:07:51.84	21.028 ± 0.005	–	68^{+12}_{-12}	$0.073^{+0.011}_{-0.011}$	14^{+4}_{-4}	$0.05^{+0.03}_{-0.03}$
G3	06:00:08.32	−20:07:52.54	20.417 ± 0.005	0.4316 ± 0.0002	184^{+12}_{-30}	$0.166^{+0.022}_{-0.008}$	47^{+7}_{-12}	$1.16^{+0.38}_{-0.70}$
G4	06:00:09.04	−20:08:08.78	20.902 ± 0.004	0.4369 ± 0.0002	116^{+9}_{-13}	$0.113^{+0.010}_{-0.007}$	27^{+4}_{-5}	$0.26^{+0.09}_{-0.12}$
G5	06:00:06.69	−20:08:14.93	20.919 ± 0.005	0.4307 ± 0.0002	265^{+11}_{-12}	$0.225^{+0.004}_{-0.005}$	73^{+10}_{-12}	$3.75^{+1.08}_{-1.29}$
G6	06:00:07.58	−20:08:40.14	21.143 ± 0.006	–	233^{+25}_{-39}	$0.202^{+0.027}_{-0.017}$	63^{+12}_{-16}	$2.47^{+1.05}_{-1.50}$
G7	06:00:09.95	−20:07:21.31	21.107 ± 0.005	–	97^{+45}_{-22}	$0.098^{+0.018}_{-0.038}$	22^{+13}_{-7}	$0.15^{+0.22}_{-0.12}$
G8	06:00:09.85	−20:08:03.68	21.266 ± 0.004	–	216^{+8}_{-13}	$0.190^{+0.007}_{-0.004}$	57^{+8}_{-10}	$1.95^{-0.55}_{-0.71}$
G9	06:00:05.38	−20:08:36.60	21.312 ± 0.005	–	222^{+11}_{-13}	$0.194^{+0.007}_{-0.006}$	59^{+8}_{-10}	$2.11^{+0.63}_{-0.79}$
G10	06:00:10.66	−20:06:50.65	20.144 ± 0.003	–	220^{+14}_{-13}	$0.193^{+0.007}_{-0.009}$	59^{+9}_{-10}	$2.06^{+0.67}_{-0.75}$
G11	06:00:09.58	−20:07:00.54	20.271 ± 0.004	0.4439 ± 0.0002	392^{+15}_{-17}	$0.311^{+0.005}_{-0.007}$	118^{+16}_{-19}	$13.15^{+3.75}_{-4.50}$
G12	06:00:19.94	−20:06:44.71	20.305 ± 0.014	–	293^{+23}_{-26}	$0.244^{+0.016}_{-0.015}$	83^{+13}_{-16}	$5.16^{+1.85}_{-2.15}$
G13	06:00:20.40	−20:06:39.98	21.029 ± 0.014	–	119^{+26}_{-12}	$0.115^{+0.009}_{-0.021}$	28^{+8}_{-6}	$0.28^{+0.21}_{-0.13}$
G14	06:00:13.96	−20:07:27.66	21.762 ± 0.005	–	214^{+8}_{-7}	$0.173^{+0.004}_{-0.005}$	60^{+4}_{-3}	$2.00^{+0.28}_{-0.26}$

Notes.[a] Fixed to the SEXTRACTOR-measured values.

[b] Scaled to the galaxy luminosity using the relations (5)–(7).

[c] Weight of the galaxy is a free parameter in the SL model (Section 3.3).

[d] Core radius is a free parameter in the SL model (Section 3.3).

Note. *Column 1*: Galaxy designation. *Columns 2 and 3*: right ascension and declination. *Column 4*: observed *r*- or *F606W*-band magnitude from our GMOS imaging or the RELICS catalogue. *Column 5*: spectroscopic redshift from either the GMOS, MUSE, or DEIMOS spectroscopy. *Column 6*: velocity dispersion of the dPIE profile. *Column 7*: core radius of the dPIE profile. *Column 8*: truncation radius of the dPIE profile. *Column 9*: total mass of the dPIE profile computed from the model parameters.

As explained in more detail in section 3.4 in Furtak et al. (2023a), the code optimizes the model by minimizing the source plane χ^2, defined as follows:

$$\chi^2 = \sum_i \frac{\left(\vec{\beta}_i - \vec{\beta}_0\right)^2}{\mu_i^2 \sigma_i^2}, \qquad (8)$$

where $\vec{\beta}_i$ represents the source position of each multiple image, $\vec{\beta}_0$ the common modelled barycentre source position of the images belonging to the same system, and μ_i and σ_i, respectively, the magnification and positional uncertainty of each multiple image. In principle, this method performs as well as a minimization in the lens plane (Keeton 2010) while being significantly faster in terms of computation time. Note that since our model is constrained with the point positions and redshifts of multiple images, and not with surface brightness distributions, we are not concerned about degeneracies between small-scale mass–density perturbations and source properties (e.g. Wagner 2022) for the scope of this work. The minimization is performed by first running 35 relatively short Monte Carlo Markov Chains (MCMC) of ∼ 10^3 steps each to crudely sample the parameters space and estimate the covariance matrix, and then refining the result in a longer MCMC chain with several 10^4 steps and decreasing 'temperature' to effectively enable annealing.

4 RESULTS

The results of our analysis of MACS0600 and its extended eastern structures are presented in the following text. In Sections 4.1 and 4.2, we summarize the discovery of the eastern structure presented in this work in the optical, X-ray, and SZ analyses of the cluster. In Section 4.3, we present the results of the SL mass modelling analysis of the extended MACS0600 field.

4.1 Optical detection of the extended structures

As introduced in Section 2, a significant mass outside of the cluster was first suspected due to difficulties in reproducing the strongly lensed multiple images in the *HST* field of view of MACS0600. First mass models for the cluster based on *HST*/RELICS and the shallow VLT/MUSE data available at the time (see Section 2.4) were presented in the works that first investigated the quintuply-imaged $z = 6.07$ galaxy, Fujimoto et al. (2021) and Laporte et al. (2021) (see also the discussion in Section 5.1), and required a strong external shear component to properly explain the multiple images. This was perhaps most strongly noted by the model using the Light-Traces-Mass method (LTM; Zitrin et al. 2015), in which the mass distribution follows the cluster galaxy distribution in the field of view such that no intrinsic ellipticity is assigned, making it susceptible to outside massive structures which contribute
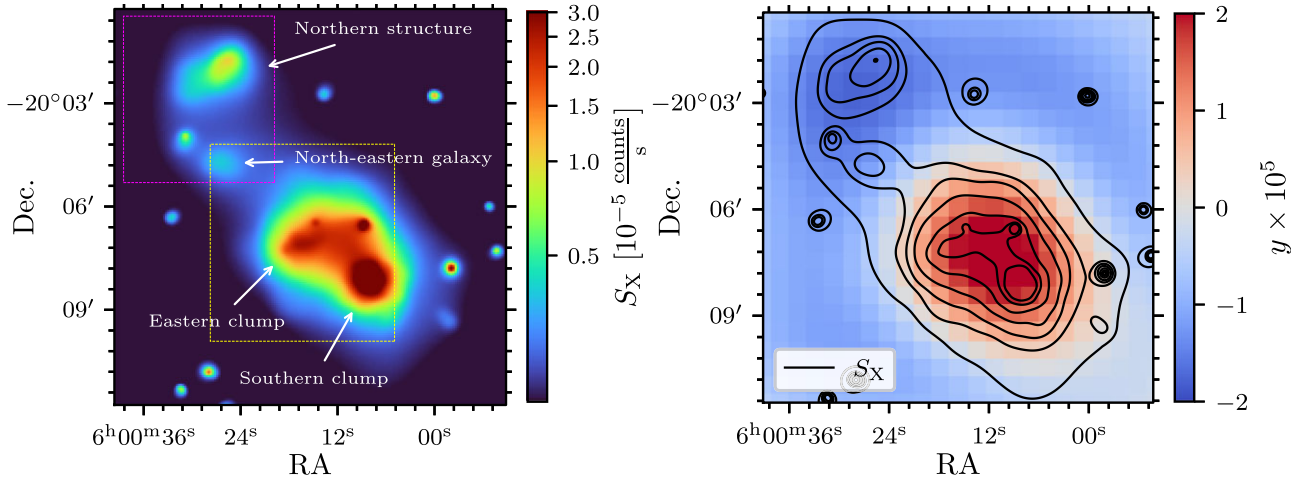
Figure 6. *Left*: X-ray surface brightness map of MACS0600 observed with *XMM–Newton* (Section 2.6). The yellow rectangle roughly outlines the area shown in the *Gemini + HST* colour image in Fig. 1 and the purple rectangle the area shown in Fig. 9. In bulk, the overall intra-cluster gas distribution follows the boot-leg shape of the SL-constrained total mass distribution. The X-ray point source on the western halo is a bright foreground star. Additional X-ray-emitting structures in the far north of the cluster suggest additional massive cluster structures beyond the field of view of our optical observations. *Right:* SZ Compton-y map of MACS0600 computed from the ACT and *Planck* data (Section 2.6) and smoothed with a 3×3 pixel Gaussian kernel. The black contours represent the X-ray surface brightness in the same steps as shown in Fig. 1. The SZ signal is centred on the barycentre between the eastern, western, and southern clumps. The additional northern structures seen in the X-ray map do not appear in the combined ACT and *Planck* SZ map, suggesting that they are below the mass limit of the ACT survey in that sky region, i.e. $M_{500,\mathrm{SZ}} < 4 \times 10^{14}\,\mathrm{M}_\odot$.

to the overall lensing signal. While recent works have found that external shear components in SL can possibly arise due to several factors that do not necessarily involve additional cluster structure beyond the field of view (Lin, Wagner & Griffiths 2023; Etherington et al. 2024), in this particular case some shallow ground-based imaging data were available (see Section 2.6) and indeed hinted at possible cluster structures outside *HST*'s field of view.

To verify this, we obtained deep optical imaging and spectroscopy with *Gemini-N*/GMOS (Section 2.1). The GMOS imaging indeed reveals a prominent overdensity of cluster galaxies north-east of the RELICS field of view (Fig. 1). Our GMOS spectroscopy, together with the *Keck*/DEIMOS spectroscopy (Sections 2.1 and 2.5), confirms the newly discovered eastern structure to lie at the same redshift as the previously observed parts of MACS0600: the redshifts of the two eastern BCGs (BCG1 and BCG2) are $z = 0.4403 \pm 0.0001$ and $z = 0.4357 \pm 0.0002$, respectively (see also Table 2). As discussed in detail in Section 3.1, 11 additional cluster member galaxies in the eastern part were spectroscopically confirmed to lie at the cluster redshift as well.

Using the 67 spectroscopic redshift measurements of cluster members (see Section 3.1), we can estimate the velocity dispersions of the cluster substructures. In order to do that, we assign each galaxy with a spectroscopic redshift measurement to one of the substructures by determining which BCG it lies closest to and thus obtain tentative velocity dispersions of $\sigma_{v,\mathrm{east}} = (1276 \pm 203)\,\frac{\mathrm{km}}{\mathrm{s}}$, $\sigma_{v,\mathrm{south}} = (1316 \pm 146)\,\frac{\mathrm{km}}{\mathrm{s}}$, and $\sigma_{v,\mathrm{west}} = (506 \pm 132)\,\frac{\mathrm{km}}{\mathrm{s}}$ for the eastern, southern, and western substructures, respectively. The uncertainties are computed with a jackknife sampling method. These results indicate that the eastern structure is probably at least as massive as the previously known southern and western clumps. Note however that these estimates are based only on a handful of spectroscopic redshifts in each clump and can therefore only be seen as very rough first-look estimates.

4.2 The extended intra-cluster gas

We analyse the morphology of the hot ICM gas in MACS0600 through both X-ray observations and the SZ effect.

The X-ray surface brightness map is constructed from the *XMM–Newton* data (Section 2.6). We show the cluster's extended X-ray surface brightness in the left-hand panel of Fig. 6. The bulk of the X-ray emission is located at the position of the southern DM halo. The overall distribution however follows a boot-leg shape, similar to the cluster member distribution and our SL model mass distribution (Fig. 1), with an overdensity that corresponds to the eastern DM haloes. Note that there seems to be an X-ray point source in the western DM halo which concurs spatially with a bright foreground star (see Fig. 1). While the southern component is brightest in X-rays, it is probably slightly less massive than the eastern clump. Its temperature profile decreases from $T_{\mathrm{X}} = (8.3 \pm 0.5)$ to $T_{\mathrm{X}} = (6.3 \pm 0.4)\,\mathrm{keV}$ towards its core, whereas the eastern clump has a very high temperature of $T_{\mathrm{X}} > 9\,\mathrm{keV}$ and up to $T_{\mathrm{X}} = (10.0 \pm 0.6)\,\mathrm{keV}$. This suggests that the eastern halo is slightly more massive, whereas the southern structure is in a less advanced stage of merging, since it still has a well-defined cool core. Note that this also concurs with the results of our SL modelling analysis as described in Section 4.3.

Interestingly, there is a distinct (i.e. $\sim 30\sigma$ detected) extended X-ray structure located far outside even the *Gemini*/GMOS field of view, ~ 5 arcmin from BCG1 (corresponding to $\sim 1.7\,\mathrm{Mpc}$ at $z_{\mathrm{d}} = 0.43$). This strongly hints at further massive cluster structures associated with MACS0600 beyond those discovered using GMOS imaging in this work, even though at present it is not possible to precisely determine if this northern structure lies at the same redshift as the cluster since we do not detect any X-ray emission lines. That being said, we find an overdensity of probable cluster galaxies in that area in the wide-field VIRCAM observations (see Section 2.6) which we discuss in detail in Section 5.2. In addition, there is another smaller and more diffuse X-ray overdensity that corresponds to the position of the bright north-eastern galaxy seen in the corner of the GMOS

imaging (Section 3.1 and Fig. 1), which is in the middle between the eastern clump and the additional northern structure seen in the X-ray map. The northern X-ray-emitting structure has a temperature of $T_X = (4.5 \pm 0.3)$ keV, which indeed confirms it to be a massive cluster-like structure. The smaller diffuse X-ray overdensity on the north-eastern BCG is somewhat cooler with a temperature of $T_X = (3.5 \pm 0.2)$ keV. Finally, we note that the X-ray surface-brightness map also shows several point sources, some of them perhaps quasars, located around the cluster.

For examining the cluster's SZ signal, we create a combined SZ-map from the two mm-wave frequency channels from the ACT and *Planck* maps (see Section 2.6). We convert both maps to units of the SZ Compton-y parameter and smooth the 150 GHz map to an effective FWHM of 2.1 arcmin. Then, we compute the inverse-variance weighted average of the two maps. The resulting combined y-map is shown in the right-hand panel of Fig. 6, overlaid with the X-ray surface-brightness contours. The SZ-signal agrees with the location of the total mass distribution of the cluster, but the spatial resolution is not high enough to show if it is centred on any particular sub-halo. There is none the less clearly a contribution from the massive eastern structure, as the signal seems to be centred on the barycentre between the southern, western, and eastern clumps. The extended structures to the far north, seen in the X-ray map, do not appear in the SZ map. Given the mass-limit of the ACT survey in this region of the sky (Hilton et al. 2021), we therefore place a conservative upper limit on the total mass of the northern structures based on the ACT survey limit it that sky region, i.e. $M_{500,SZ} < 4 \times 10^{14}$ M$_\odot$, consistent with the lower X-ray temperatures. The SZ-derived total mass of the cluster from ACT is $M_{500,SZ} = (9.7 \pm 1.7) \times 10^{14}$ M$_\odot$ (Hilton et al. 2021) and from *Planck* is $M_{500,SZ} = (10.7 \pm 0.5) \times 10^{14}$ M$_\odot$ (Planck Collaboration XXVII 2016).

4.3 SL mass model

We construct an SL model for the extended MACS0600 field, including the massive eastern structure. While the shape of the model around the eastern part is based largely on photometric multiple-image candidates identified in the *Gemini* data from the ground and thus requiring further verification, the model suggests that, in line with its optical luminosity density, ICM gas signatures, and velocity dispersion, the eastern part is indeed very massive and contributes significantly the lensing signal.

The final SL model of the cluster has an average *lens* plane image reproduction error (RMS; root of mean squares) of $\Delta_{RMS} = 0.72$ arcsec which corresponds to a lens plane $\chi^2 = 171$. Given the 93 SL constraints and 52 free parameters employed, which result in 41 degrees of freedom, this translates to a reduced χ^2 of $\simeq 4.2$. Note that the RMS is mostly driven by the heavily underconstrained eastern part of the cluster. The RMS of multiple images located in the *HST*- and MUSE-observed western and southern parts of the cluster (see Fig. 5) is $\Delta_{RMS,SW} = 0.23$ arcsec. In particular, system 7, the $z = 6.072$ quintuply-imaged system further analysed in Fujimoto et al. (2024), is very well reproduced with an average reproduction error $\Delta_{RMS,7} = 0.12$ arcsec between its five images. This means that the well-constrained previously known substructures of the cluster are exceptionally well reproduced by our model.

The critical curves for sources at $z_s = 2.01$ and $z_s = 10$ are shown overlaid over the cluster in Fig. 1 and again in Fig. 5. The presented model comprises a total critical area of $A_{crit} \simeq 2.16$ arcmin^2 which translates to an effective Einstein radius of $\theta_E = 49.7$ arcsec ± 5.0 arcsec, for a source at $z_s = 2$, the second largest observed to date after MACS J0717.5+3745
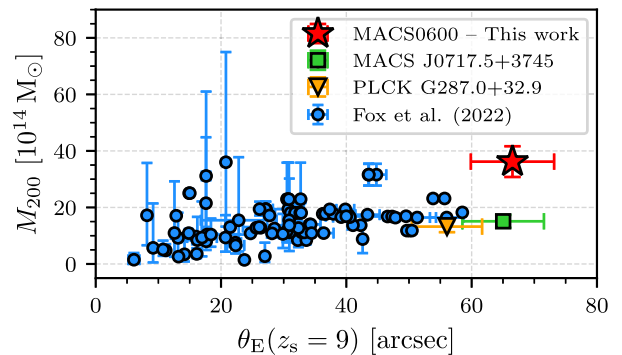
Figure 7. Cluster mass M$_{200}$ in relation to the effective Einstein radius for a source at $z_s = 9$. Our results for MACS0600 are shown in red and we also show the equivalent values for the two massive clusters MACS J0717.5+3745 (Zitrin et al. 2015) and PLCK G287.0+32.9 (Zitrin et al. 2017) in green and orange, respectively. For comparison, the Fox et al. (2022) sample of 74 clusters is shown in blue. With the addition of the eastern structures, MACS0600 clearly ranges among the largest and most massive galaxy clusters known to date.

($\theta_E = 55$ arcsec ± 3 arcsec; e.g. Zitrin et al. 2009). The enclosed total mass is then $M(< \theta_E) = (4.7 \pm 0.7) \times 10^{14}$ M$_\odot$. The southern and western substructures, which were previously known from the RELICS observations, have a critical area of $A_{crit,sw} \simeq 0.98$ arcmin^2, with an effective Einstein radius of $\theta_{E,sw} = 33.6$ arcsec ± 3.4 arcsec enclosing $M(< \theta_{E,sw}) = (2.1 \pm 0.3) \times 10^{14}$ M$_\odot$ for $z_s = 2$. For the same source redshift, the newly discovered eastern substructure adds $A_{crit,east} \simeq 1.17$ arcmin^2 to the critical area, with $\theta_{E,east} = 36.6$ arcsec ± 3.7 arcsec enclosing $M(< \theta_{E,east}) = (2.6 \pm 0.4) \times 10^{14}$ M$_\odot$. This means that the addition of the eastern structures to the SL model of MACS0600 essentially doubles its critical area. We warrant however that these numbers are still uncertain because our model is poorly constrained in the eastern part due to lack of space-based imaging and secure multiple image identification.

Summing the surface mass density over the whole field of the current SL model (corresponding to the GMOS field of view shown e.g. in Figs 1 and 2), we obtain a total projected cluster mass M_{SL}. Given the size of our field of view and the typical values for r_{200} of massive galaxy clusters (e.g. Merten et al. 2015), this is comparable to an M_{200} mass. The result is $M_{SL} = (3.6 \pm 0.5) \times 10^{15}$ M$_\odot$, which makes MACS0600 one of the most massive clusters known to date. It also agrees with the SZ masses derived in Section 4.2 given typical ratios between M_{200} and M_{500} (Merten et al. 2015). For comparison, we plot our total cluster mass against the effective Einstein radius (for high-redshift sources in this case) in Fig. 7, compared to ~ 75 other massive SL clusters from the literature. As can be seen, MACS0600 is possibly the most extreme case thus far. That being said, we note that while some of the clusters in the Fox et al. (2022) sample have been found to have associated massive structures outside their field of view, e.g. Abell 2744 (e.g. Jauzac et al. 2016; Mahler et al. 2018; Furtak et al. 2023a), the sample is based on the publicly available SL models which concentrate on small fields of view of the cluster centres and would therefore not be sensitive to further extended structures.

The resulting smooth cluster DM halo PIEMD (1) parameters of the model are presented in Table 3. The most massive single halo is the southern sub-clump and it is also the best constrained since all of the spectroscopic multiple images to date are located in this part of the cluster. The western halo is very elliptical, which also agrees with the projected distribution of cluster galaxies in that area. The two eastern haloes, representing the extended substructures discovered

Table 3. Median DM halo PIEMD parameters, defined in equations (1) and (3) in Section 3, and their 1σ-errors for our SL model of MACS0600.

Halo	RA	Dec.	ϵ	θ (deg)	σ_v ($\frac{\mathrm{km}}{\mathrm{s}}$)	r_{core} (kpc)
			Eastern structure			
East-1	$06{:}00{:}19.47^{+0.02}_{-0.01}$	$-20{:}06{:}45.42^{+0.86}_{-1.57}$	$0.819^{+0.002}_{-0.003}$	$3.8^{+0.2}_{-0.1}$	742^{+28}_{-27}	12^{+2}_{-3}
East-2	$06{:}00{:}16.81$	$-20{:}06{:}55.65$	$0.336^{+0.012}_{-0.020}$	$72.7^{+2.1}_{-2.9}$	807^{+33}_{-18}	28^{+2}_{-2}
			RELICS MACS0600 field of view			
South	$06{:}00{:}08.16$	$-20{:}08{:}08.83$	$0.232^{+0.001}_{-0.001}$	$-65.6^{+0.8}_{-1.3}$	1203^{+18}_{-13}	74^{+4}_{-3}
West	$06{:}00{:}10.23$	$-20{:}07{:}02.35$	$0.531^{+0.012}_{-0.009}$	$-0.7^{+0.4}_{-0.3}$	795^{30}_{-25}	93^{22}_{-15}

Note. Column 1: DM halo designation. *Columns 2 and 3*: right ascension and declination. One of the eastern haloes and the southern and western haloes are fixed to their BCG positions (see Section 3.3). *Column 4*: ellipticity ϵ defined in equation (4). *Column 5*: position angle, counter-clockwise with respect to the east–west axis. *Column 6*: velocity dispersion of the PIEMD profile. *Column 7*: core radius of the PIEMD profile.

in this work, are together again as massive as the previously known southern and western structures. These results are further discussed in Section 5.

The resulting dPIE parameters (2) of the BCGs and galaxies with a free weight in the model are listed in Table 2. For the reference galaxy of luminosity $L_\star$, corresponding to $M = -21.04$ (see Section 3.3), our model finds $\sigma_{v,\star} = 230^{+7}_{-9}\,\mathrm{km\,s^{-1}}$ and $r_{\mathrm{cut},\star} = 62^{+8}_{-10}$ kpc. The resulting luminosity scaling relation exponents from equations (5) to (7) are $\lambda = 0.488^{+0.004}_{-0.003}$, $\beta = 0.406^{+0.003}_{-0.005}$, and $\alpha = 0.592^{+0.003}_{-0.003}$. This roughly agrees with typical values for λ, for example, measured with internal kinematic stellar modelling of cluster galaxies ($\simeq 0.4$, e.g. Bergamini et al. 2019, 2021, 2023).

Finally, the redshifts predicted by the model for the systems whose redshifts were left as free parameters (see Section 3.3) are listed in Table A1 in Appendix A. We in particular note that the two new systems 27 and 30, which were identified in the *JWST*/NIRCam imaging, are predicted at relatively high redshifts of $z_{\mathrm{model}} = 7.0^{+0.1}_{-0.2}$ and $z_{\mathrm{model}} = 6.7^{+0.2}_{-0.3}$, respectively. For system 27, this is consistent with a non-detection in even the deep MUSE data available since the instrument can only detect the Lyman α line out to $z = 6.7$ and the *HST*/WFC3 data are probably too shallow (0.5 orbits) to detect this system. System 30 on the other hand lies outside of both the MUSE and WFC3 fields of view (see Fig. 2) and would therefore not have been detected previously.

5 DISCUSSION

The optical, ICM, and SL analyses described in Section 4 reveal a previously un-noted massive structure associated with MACS0600, making it one of most massive galaxy clusters studied to date. The model also suggests that it is possibly the cluster with the second-largest Einstein radius ($\theta_{\mathrm{E}} \simeq 49$ arcsec, for a source at $z_s = 2$), which could in turn become the largest Einstein radius cluster for high-redshift sources at $z \sim 9$–10 (see Fig. 7). In this section, we place these results into context and discuss them with regard to previous SL models and SL modelling systematics (Section 5.1), the large-scale structure around the cluster (Section 5.2), and the prospects for future high-redshift surveys using the SL magnification of the cluster (Section 5.3).

5.1 Limits of the SL model and comparison to the literature

Previous SL models of MACS0600 were published in Laporte et al. (2021) and Fujimoto et al. (2021) and include two parametric models with GLAFIC (Oguri 2010) and lenstool (Kneib et al. 1996;

Jullo et al. 2007; Jullo & Kneib 2009), and an LTM model. Another lenstool parametric model can be found in the public RELICS repository (Fox et al. 2022). These models were typically based on 10 multiple image systems (systems 1–10 in Table A1) known from the RELICS *HST* imaging, with seven spectroscopic redshifts from ALMA, GMOS, and the shallow MUSE data available at the time (see Section 2.4), and limited to the southern and western haloes covered by *HST*. The public RELICS lenstool model was constrained with six multiple image systems and five spectroscopic redshifts. Similar to our model, the previous models assumed two or three smooth DM haloes to represent the western and southern haloes. The model we present here covers the newly discovered eastern structures, and uses additional multiple images and spectroscopic redshifts now available in the original *HST* region (see Fig. 5).

The main limit of our extended SL analysis is the lack of high-resolution imaging around the eastern haloes. While our results for the western and southern haloes broadly concur with the literature models mentioned above, the two eastern haloes are largely under-constrained, containing only four multiple-image candidate systems (see Fig. 5) and none of them with spectroscopic redshifts. This drives the total average RMS of our SL model $\Delta_{\mathrm{RMS}} = 0.72$ arcsec since the lens-plane RMS is known to often become larger when less spectroscopic multiple image systems are used (e.g. Johnson & Sharon 2016). Indeed, the RMS of our model in the western and southern regions of the cluster that are covered by *HST* and MUSE is much better: $\Delta_{\mathrm{RMS,SW}} = 0.23$ arcsec. The lack of SL constraints in the eastern area might also explain why the first eastern halo strays far from its main BCG, and its somewhat extreme ellipticity (Table 3). Despite this uncertainty, in terms of total SL mass the eastern substructure is predicted to be as or more massive than the previously known parts of MACS0600, essentially doubling the cluster's total mass as shown in Section 4.3. This is consistent also with the X-ray temperatures, which suggest that the eastern structure is possibly the more massive one.

To further assess the size of the eastern clumps and the robustness of GMOS-detected multiple image systems in the eastern haloes and their affect on the results, we exploit the predictive power of the LTM method (Zitrin et al. 2015; Carrasco, Zitrin & Seidel 2020). We run an LTM SL model using the secure multiple image systems in the western and southern haloes and the full cluster member catalogue assembled in Section 3.1, but not using any of the eastern multiple images that were only identified in the ground-based data and thus remain uncertain. Using the light distribution of cluster members in the eastern part of the cluster alone, the LTM model ($\Delta_{\mathrm{RMS}} = 2.1$ arcsec) indeed predicts there to be a significant
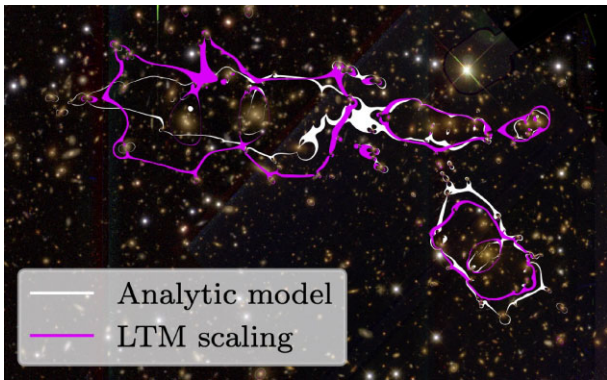
Figure 8. Critical lines for a source at $z_s = 2.01$ of our analytic SL model presented in Section 4.3 (white) and of the LTM model run with only the western multiple images (magenta). The cut-out shown here is the same field of view as Fig. 5. While no multiple images in the eastern part were used for that model, the LTM model clearly predicts a supercritical massive SL structure that concurs with our eastern haloes. A full-resolution (0.06 arcsec pix^{-1}), fully vectorized version of this figure is included in the online supplementary material of this paper.

supercritical SL cluster structure around the two eastern BCGs where we placed the eastern haloes in our analytic model (Sections 3.3 and 4.3), and with similar symmetry, as can be seen in Fig. 8. Finally, for further verification, we rerun our parametric model with the same configuration but without including the eastern multiple images. This model also achieves an RMS of $\Delta_{RMS} = 0.2$ arcsec. While the individual parameters of the eastern haloes are very different than those of our results presented in Section 4.3 and Table 3, on account of being completely unconstrained, the overall properties such as the effective Einstein radius, enclosed mass, and total cluster mass only vary marginally and agree within 1σ. The results in the southern and western haloes from this model also agree with our total model, further confirming that this part of the cluster is well constrained.

In order to better constrain the SL mass profile of the eastern structures, high-resolution space-based observations with *HST* and *JWST* to detect more and more robust multiple images and arcs in the eastern part of the cluster would be required. Additional spectroscopic coverage of both the western and eastern haloes would also be needed to derive spectroscopic redshifts of new multiple image systems and optimally constrain the total mass distribution of the cluster with SL mass modelling.

5.2 Further surrounding large-scale structure

As shown in Figs 1 and 6, our analysis finds MACS0600 to be a very large and complex merging galaxy cluster structure, mostly extending along the north-east to south-west direction. While the X-ray analysis described in Section 4.2 clearly detects another large cluster-scale emission feature in the north, the absence of X-ray emission lines does not enable us to confirm that it lies at the same redshift of $z_d = 0.43$ of the cluster.

We instead use the wide-field VIRCAM observations (see Section 2.6) to search for cluster galaxies in or around this X-ray overdensity. A VIRCAM colour-composite image of the northern X-ray emission feature is shown in Fig. 9. The VIRCAM image clearly shows a number of large elliptical galaxies with similar colours as our cluster members in the vicinity of the X-ray emission. For a more quantitative assessment, we run SEXTRACTOR to detect sources and measure photometry in the three VIRCAM bands and then select
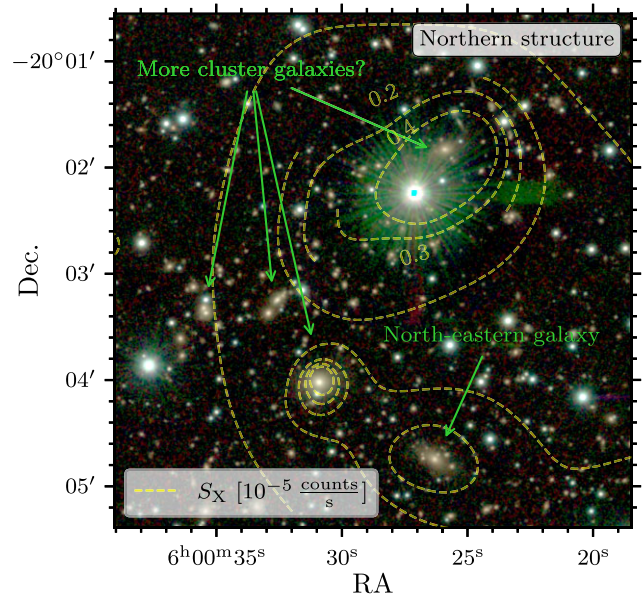

Figure 9. A 4.8 arcmin $\times$ 4.8 arcmin cut-out of the VIRCAM colour-composite image used in Fig. 2 (blue: *Y* band, green: *J* band, red: *Ks* band) showing the northern X-ray emission structure (see left-hand panel of Fig. 6). The X-ray surface-brightness contours are overlaid in yellow as in Fig. 1. The X-ray emission in this region concurs with an overdensity of galaxies that match the colours of cluster members, suggesting that it likely lies at the same redshift as the cluster.

potential cluster galaxies in colour–magnitude and colour–colour space by calibrating our selection to the VIRCAM colours of our cluster member catalogue assembled in Section 3.1. Given the shallow depth of the VIRCAM observations (23.5 mag at 5σ), we select galaxies brighter than 23 mag for this analysis. While NIR data are not optimal to select cluster galaxies at $z_d = 0.43$, since the 4000 Å-break falls in optical wavelengths, from the ancillary data listed in Section 2.6, the VIRCAM imaging achieve sufficient resolution and depth in a wide field around the cluster. Moreover, our selection recovers all of the spectroscopic and optical photometric cluster members that are bright enough to be robustly detected. This selection indeed confirms most of the galaxies seen in Fig. 9 to have the same VIRCAM colours as our cluster members. Furthermore, the resulting luminosity surface density of cluster members, as shown in Fig. 10, clearly presents an overdensity in the north-east, outside the field of view of our optical imaging. Overall, the luminosity density distribution is complex, mostly elongated in the north-east to south-west direction and with perhaps another branch in the north-western direction. This suggests that MACS0600 and its extended structures form a node of the cosmic web with filaments branching out. Similar structures have been found around other very massive galaxy clusters, most prominently MACS J0717.5+3745 (e.g. Jauzac et al. 2012, 2018; Durret et al. 2016; Ellien et al. 2019).

We also note that the additional northern structure lies at $\sim$ 5 arcmin ($\sim$ 1.7 Mpc) from BCG1, which means that it could be targeted in the parallel field of *HST* if the primary field is aimed at the eastern haloes. Future high-resolution *HST* imaging programs of the eastern extension of MACS0600 could therefore also target the northern structures in the same visit, potentially yielding two large SL fields simultaneously at minimal cost.

As was shown by e.g. Acebron et al. (2017) and Mahler et al. (2018), massive structures far from the cluster centre can also
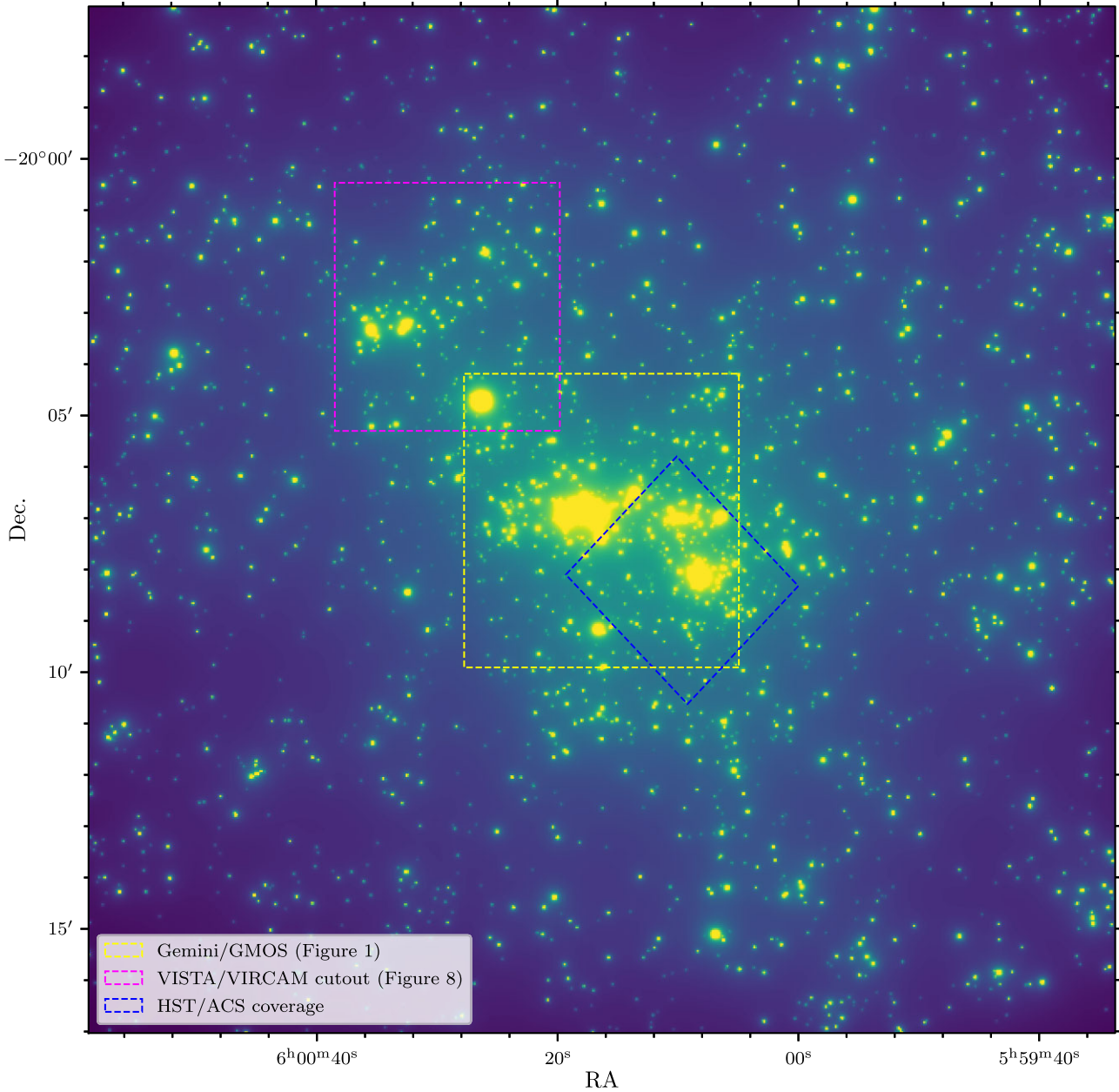
Figure 10. VIRCAM *Y*-band luminosity density of cluster member galaxies in a wide 20 arcmin × 20 arcmin area around MACS0600. At $z_d = 0.43$, one arcminute corresponds to 0.34 Mpc. While some 60 galaxies were verified spectroscopically (see Section 3.1), most of the cluster members were selected photometrically, some only in the VIRCAM imaging data with poor colour range, and should thus be referred to as mere candidates. The yellow square represents the area shown in Fig. 1, the magenta square the area shown in Fig. 9, and the blue square the previously known part of the cluster with RELICS *HST* coverage. The cluster member luminosity distribution presents an overdensity at roughly the same location as the northern X-ray structures shown in Figs 6 and 9, indicating that it indeed most likely lies at the same redshift and is associated with the cluster. Elongations of the luminosity density in the north-east to south-west, and tentatively towards the north-west direction, indicate filamentary structures with the cluster embedded in a node of the cosmic web.

significantly affect the SL signal. Thus, the tentative northern structure may affect the multiple image formation in the cluster core to some extent. In that sense we note, however, that an alternative version of our model, run with an external shear component included, did not significantly impact the results or the multiple image reproduction, suggesting that the contribution from that tentative northern clump on the main SL regime would probably be minor. This may however also be a result of the low number and generally high uncertainty of the eastern multiple image systems, which make it impossible to determine if an external shear is currently required since the model is already underconstrained in that area.

5.3 Prospects for high-*z* galaxy observations

With its exceptionally large critical area, of 2.16 arcmin^2 at $z_s = 2$ (see Section 4.3) and 3.91 arcmin^2 at $z_s = 10$, MACS0600 represents an excellent field for future studies of the high-redshift Universe using its SL magnification. Indeed, SL cluster fields have been proven invaluable to the study of faint and low-mass objects at high redshifts
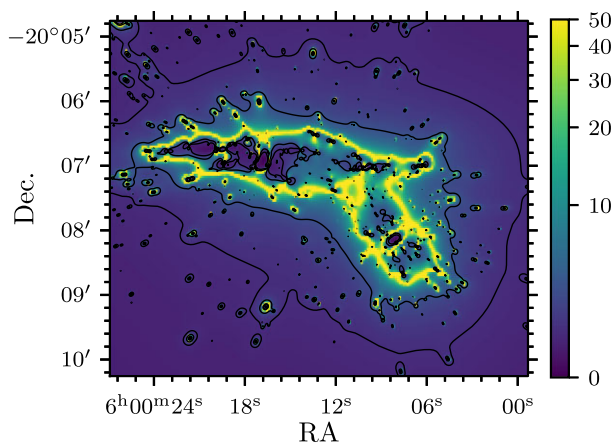
Figure 11. Magnification map of our SL model of MACS0600 for a source at $z_s = 10$. The black contours represent magnifications of $\mu = 2$ and $\mu = 4$. The combination of the substructures in MACS0600 forms a large area of high magnification, making the cluster particularly well suited to probe the high-redshift Universe as a cosmic telescope.
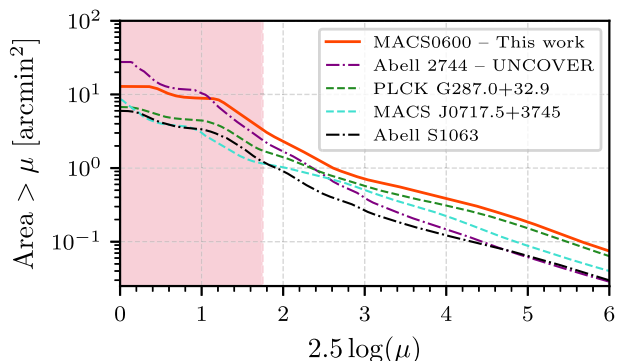
Figure 12. Cumulative source plane area at $z_s = 10$ as a function of magnification. Our model of MACS0600 is shown in red and we compare it to models of other very large SL clusters, namely the UNCOVER Furtak et al. (2023a) model of Abell 2744, the Zitrin et al. (2017) LTM model of PLCK G287.0+32.9, and LTM models of MACS J0717.5+3745 and Abell S1063 (Zitrin et al. 2015) for reference. While the low-magnification end ($\mu \lesssim 5$, red shaded area) depends only on the size of the observed field, the high-magnification fraction of the source plane area is largely independent of that. In this regime, MACS0600 has the largest source plane areas according to our model.

both with *HST* (e.g. Bouwens et al. 2017; Atek et al. 2018; Ishigaki et al. 2018; Strait et al. 2020, 2021; Furtak et al. 2021) and *JWST* (e.g. Adams et al. 2023; Atek et al. 2023a, 2024a; Bouwens et al. 2023; Bradley et al. 2023; Harikane et al. 2023).

To illustrate that MACS0600 is a promising field for deep high-redshift observations, we show the $z_s = 10$ magnification map and cumulated source-plane area as a function of magnification in Fig. 11, and compare the latter to several other large cluster lenses. The four haloes probed in our SL model form a contiguous sheet of high magnification and the high-magnification ($\mu \gtrsim 5$) area in the source plane clearly exceeds even the multiple SL cores of Abell 2744 observed with the *JWST Ultradeep NIRSpec and NIRCam ObserVations before the Epoch of Reionization* survey (UNCOVER; Bezanson et al. 2022), the largest SL field observed to date with *JWST*. In general, as can be seen in Fig. 12, the model of MACS0600 reveals it to present cumulated high-magnification $z_s = 10$ source-plane areas of the same order of magnitude as the most massive

known clusters, e.g. MACS J0717.5+3745 (e.g. Zitrin et al. 2009) and PLCK G287.0+32.9 (Zitrin et al. 2017; D'Addona et al. 2024), and much larger than other more typical clusters such as Abell S1063 (e.g. Zitrin et al. 2015). While the magnification areas are also strongly dependent on the lens modelling method used (e.g. Bouwens et al. 2017; Atek et al. 2018), this is nevertheless indicative that MACS0600 ranges among the most efficient cluster lenses in terms of high-magnification area. Note that in the low-magnification regime, the cumulated source plane area is not dominated by the SL region but by the total survey area, which is much larger (i.e. ~ 35 arcmin^2; Atek et al. 2023b) in the UNCOVER survey than in this work. Indeed, our conclusions are based on the current model which is in part based on candidate multiple images requiring verification. Nevertheless, even if the currently implied large critical area of MACS0600 is found to be somewhat overestimated, the existence of the massive eastern structure necessarily boosts the area of high magnifications.

We also note that the southern halo of MACS0600 alone contains a spectacular quintuply-imaged and ALMA-detected $z = 6$ disc galaxy (Fujimoto et al. 2024), and likely two more multiply-imaged $z > 6$ objects (see Section 4.3 and Table A). The RELICS *HST* data of the cluster yielded a total of eight $z \gtrsim 6$ objects (Salmon et al. 2020). This all suggests that MACS0600 covers a rich volume of the high-redshift Universe and that many more high-redshift objects may lie behind the eastern haloes and be magnified by them. Finally, with the northern potential SL structure, discovered in the X-ray emission (see Sections 4.2 and 5.2), in range of the *HST* parallel field, the extended structures of the cluster represent an excellent target for the next generations of deep *HST* and *JWST* surveys.

6 CONCLUSION

We present a new optical, X-ray, SZ, and lensing analysis of the massive RELICS galaxy cluster MACS0600 in which we discover and characterize an additional massive cluster structure.

In summary, our main results are the following:

(i) We discover a massive, bi-modal extended cluster structure to the north-east of the RELICS *HST* field of view of the galaxy cluster MACS0600 and confirm it to lie at the same redshift. Using spectroscopic redshifts of 67 cluster galaxies, we find an updated cluster redshift of $z_d = 0.432 \pm 0.007$.

(ii) We perform an SL analysis of the extended cluster and identify 18 new multiple image systems and candidates in new *JWST*/NIRCam imaging of the southern part of the cluster and five tentative multiple system candidates in the GMOS imaging of the eastern part. New ultra-deep VLT/MUSE observations of the southern sub-clump allow us to spectroscopically confirm 13 multiple image systems.

(iii) The newly discovered extended structure essentially doubles the cluster's critical area, to $A_{\rm crit} \simeq 2.16$ arcmin^2 for a source at $z_s = 2$, resulting in an effective Einstein radius of $\theta_E = 49.7$ arcsec $\pm$ 5.0 arcsec which encloses a total mass of $M(< \theta_E) = (4.7 \pm 0.7) \times 10^{14}$ M$_\odot$. If confirmed with further high-resolution imaging of the eastern haloes of the cluster, this would make MACS0600 the second largest SL cluster observed to date after MACS J0717.5+3745, with an exceptionally large high-magnification area. The total projected mass of the cluster in the modelled field of view is $M_{\rm SL} = (3.6 \pm 0.5) \times 10^{15}$ M$_\odot$, according to the current SL model.

(iv) The *XMM–Newton* 0.5–7 keV data revealed the cluster's hot X-ray gas to follow the same overall bootleg shape of the total mass distribution. The eastern X-ray clump has a high temperature of $T_X > 9$ keV, whereas the southern X-ray clump is cooler ($T_X \simeq 6$–8 keV)

and has a decreasing temperature gradient towards its core. This suggests that the eastern part is more massive, although less bright in X-rays, corroborating the findings of the SL analysis.

(v) The cluster is also detected in ACT + *Planck* SZ maps. Although these are of low resolution, the SZ signal is centred roughly on the barycentre of the three main (eastern, southern, and western) clumps of the cluster. The SZ-derived total mass of the cluster is $M_{500,SZ} = (9.7 \pm 1.7) \times 10^{14}$ M$_\odot$.

(vi) Further structures tentatively associated with MACS0600 are also detected 5 arcmin (1.7 Mpc) north-east of the cluster in X-rays and wide-field VISTA/VIRCAM NIR imaging. Additionally, the luminosity distribution of surrounding galaxies shows various filamentary-like structures around the cluster.

While our SL model of the eastern structures detected in MACS0600 is corroborated by both the X-ray analysis and an alternative LTM model, it nevertheless remains uncertain due to the lack of SL constraints (and spectroscopic redshifts) in that area. Future models will therefore require high-resolution space-based imaging observations with *HST* and *JWST*, and additional supporting spectroscopy, to robustly detect multiple images in that area and properly constrain the cluster's mass distribution. In addition, weak-lensing analyses in a wide field around the cluster and its associated structures in the far north, which can be done with wide-field ground-based imaging, as well as including the far northern structures in future SL analyses, would further help to constrain the total mass distribution of MACS0600. With its exceptionally large SL area, and the potential additional SL cluster structure in the north observable in parallel, the Anglerfish cluster MACS0600 represents a prime field for the next generation of ultra-deep *HST* and *JWST* surveys to probe the high-redshift Universe through its SL magnification. With their wide fields of view, upcoming space-based imaging missions such as e.g. *Euclid* and *Roman* will routinely enable the detections of massive associated cluster structures around SL clusters (e.g. Atek et al. 2024b).

DATA AVAILABILITY

The RELICS *HST* data and catalogues on which this work is based are publicly available on the MAST archive in the RELICS (Coe et al. 2019) repository for MACS0600.[5] The HAWK-I and VIRCAM data are publicly available on the ESO Science Archive[6] under program IDs 0103.A-0871(B) and 198.A-2008(E), respectively. The reduced MUSE data cubes are also available on the ESO Science Archive under program IDs 0100.A-0792(A) and 109.22VV.001(A), while high-level spectroscopy products are available on the Richard et al. (2021) Atlas of MUSE observations towards massive lensing clusters website.[7] The *JWST*/NIRCam observations are publicly available on the MAST archive under program ID GO-1567. The X-ray *XMM–Newton* data are publicly available on the *XMM–Newton* Science Archive[8] under observation IDs 0650381401 and 0827050601. The ACT maps (Naess et al. 2020) are publicly available on the LAMBDA server.[9] Additional data and reduced data products, i.e. the *Gemini-N*/GMOS and *Keck*/DEIMOS imaging and spectroscopy, will be shared by the authors on request.

REFERENCES

Acebron A., Jullo E., Limousin M., Tilquin A., Giocoli C., Jauzac M., Mahler G., Richard J., 2017, MNRAS, 470, 1809

Adams N. J. et al., 2023, MNRAS, 518, 4755

Asencio E., Banik I., Kroupa P., 2021, MNRAS, 500, 5249

Astropy Collaboration, 2013, A&A, 558, A33

---

[4] http://www.astropy.org
[5] https://archive.stsci.edu/missions/hlsp/relics/rxc0600-20/
[6] http://archive.eso.org/scienceportal/home
[7] https://cral-perso.univ-lyon1.fr/labo/perso/johan.richard/MUSE_data_release/
[8] http://nxsa.esac.esa.int/nxsa-web/#home
[9] https://lambda.gsfc.nasa.gov/product/act/actpol_prod_table.cfm

Ata M., Lee K.-G., Vecchia C. D., Kitaura F.-S., Cucciati O., Lemaux B. C., Kashino D., Müller T., 2022, Nat. Astron., 6, 857

Atek H., Richard J., Kneib J.-P., Schaerer D., 2018, MNRAS, 479, 5184

Atek H. et al., 2023a, MNRAS, 519, 1201

Atek H. et al., 2023b, MNRAS, 524, 5486

Atek H. et al., 2024a, Nature, 626, 975

Atek H. et al., 2024b, preprint (arXiv:2405.13504),

Bacon R. et al., 2010, in McLean I. S., Ramsay S. K., Takami H.eds, Proc. SPIE Conf. Ser. Vol. 7735, Ground-based and Airborne Instrumentation for Astronomy III. SPIE, Bellingham, p. 773508

Benítez N., 2000, ApJ, 536, 571

Bergamini P. et al., 2019, A&A, 631, A130

Bergamini P. et al., 2021, A&A, 645, A140

Bergamini P. et al., 2023, A&A, 670, A60

Bertin E., 2006, in Gabriel C., Arviset C., Ponz D., Enrique S.eds, ASP Conf. Ser. Vol. 351, Astronomical Data Analysis Software and Systems XV. Astron. Soc. Pac., San Francisco, p. 112

Bertin E., Arnouts S., 1996, A&AS, 117, 393

Bezanson R. et al., 2022, preprint (arXiv:2212.04026),

Bhatawdekar R., Conselice C. J., Margalef-Bentabol B., Duncan K., 2019, MNRAS, 486, 3805

Böker T. et al., 2022, A&A, 661, A82

Böker T. et al., 2023, PASP, 135, 038001

Bonafede A. et al., 2012, MNRAS, 426, 40

Borgani S., Guzzo L., 2001, Nature, 409, 39

Bouwens R. J., Oesch P. A., Illingworth G. D., Ellis R. S., Stefanon M., 2017, ApJ, 843, 129

Bouwens R. J., Illingworth G., Ellis R. S., Oesch P., Stefanon M., 2022, ApJ, 940, 55

Bouwens R., Illingworth G., Oesch P., Stefanon M., Naidu R., van Leeuwen I., Magee D., 2023, MNRAS, 523, 1009

Bradley L. et al., 2022, astropy/photutils: 1.5.0, Zenodo, Available at: https://doi.org/10.5281/zenodo.6825092

Bradley L. D. et al., 2023, ApJ, 955, 13

Brammer G., 2023, grizli, Zenodo, Available at: https://doi.org/10.5281/zenodo.8370018

Bushouse H. et al., 2024, JWST Calibration Pipeline, Zenodo, Available at: https://doi.org/10.5281/zenodo.6984365

CHEX-MATE Collaboration, 2021, A&A, 650, A104

Carrasco E. R. et al., 2010, ApJ, 715, L160

Carrasco M., Zitrin A., Seidel G., 2020, MNRAS, 491, 3778

Choi S. K. et al., 2020, J. Cosmology Astropart. Phys., 2020, 045

Coe D., Benítez N., Sánchez S. F., Jee M., Bouwens R., Ford H., 2006, AJ, 132, 926

Coe D., Bradley L., Zitrin A., 2015, ApJ, 800, 84

Coe D. et al., 2019, ApJ, 884, 85

D'Addona M. et al., 2024, A&A, 686, A4

Dalton G. B. et al., 2006, in McLean I. S., Iye M.eds, Proc. SPIE Conf. Ser. Vol. 6269, Ground-based and Airborne Instrumentation for Astronomy. SPIE, Bellingham, p. 62690X

de Lapparent V., Geller M. J., Huchra J. P., 1986, ApJ, 302, L1

Diaferio A., Geller M. J., 1997, ApJ, 481, 633

Diego J. M. et al., 2023a, preprint (arXiv:2312.11603)

Diego J. M. et al., 2023b, A&A, 672, A3

Donahue M., Voit G. M., Gioia I., Luppino G., Hughes J. P., Stocke J. T., 1998, ApJ, 502, 550

Dubois Y. et al., 2014, MNRAS, 444, 1453

Durret F. et al., 2016, A&A, 588, A69

Ebeling H., Edge A. C., Henry J. P., 2001, ApJ, 553, 668

Ebeling H., Barrett E., Donovan D., 2004, ApJ, 609, L49

Ebeling H., Barrett E., Donovan D., Ma C.-J., Edge A. C., van Speybroeck L., 2007, ApJ, 661, L33

Eckert D., Ettori S., Pointecouteau E., Molendi S., Paltani S., Tchernin C., 2017, Astron. Nachr., 338, 293

Elíasdóttir Á. et al., 2007, preprint (arXiv:0710.5636)

Ellien A., Durret F., Adami C., Martinet N., Lobo C., Jauzac M., 2019, A&A, 628, A34

Etherington A. et al., 2024, MNRAS, 531, 3684

Faber S. M. et al., 2003, in Iye M., Moorwood A. F. M.eds, Proc. SPIE Conf. Ser. Vol. 4841, Instrument Design and Performance for Optical/Infrared Ground-based Telescopes. SPIE, Bellingham, p. 1657

Finner K. et al., 2017, ApJ, 851, 46

Finner K. et al., 2021, ApJ, 918, 72

Foley R. J. et al., 2011, ApJ, 731, 86

Fox C., Mahler G., Sharon K., Remolina González J. D., 2022, ApJ, 928, 87

Frye B. L. et al., 2023, ApJ, 952, 81

Frye B. L. et al., 2024, ApJ, 961, 171

Fujimoto S. et al., 2021, ApJ, 911, 99

Fujimoto S. et al., 2023, preprint (arXiv:2303.01658),

Fujimoto S. et al., 2024, preprint (arXiv:2402.18543),

Furtak L. J., Atek H., Lehnert M. D., Chevallard J., Charlot S., 2021, MNRAS, 501, 1568

Furtak L. J. et al., 2023a, MNRAS, 523, 4568

Furtak L. J. et al., 2023b, ApJ, 952, 142

Furtak L. J. et al., 2024a, MNRAS, 527, L7

Furtak L. J. et al., 2024b, Nature, 628, 57

Gardner J. P. et al., 2023, PASP, 135, 068001

Geller M. J., Diaferio A., Rines K. J., Serra A. L., 2013, ApJ, 764, 58

Geller M. J., Hwang H. S., Fabricant D. G., Kurtz M. J., Dell'Antonio I. P., Zahid H. J., 2014, ApJS, 213, 35

Geller M. J., Hwang H. S., Dell'Antonio I. P., Zahid H. J., Kurtz M. J., Fabricant D. G., 2016, ApJS, 224, 11

Ghirardini V. et al., 2019, A&A, 621, A41

Glazebrook K. et al., 2024, Nature, 628, 277

Golubchik M. et al., 2023, MNRAS, 522, 4718

Greene J. E. et al., 2024, ApJ, 964, 39

Halkola A., Seitz S., Pannella M., 2006, MNRAS, 372, 1425

Halkola A., Seitz S., Pannella M., 2007, ApJ, 656, 739

Harikane Y. et al., 2023, ApJS, 265, 5

Hilton M. et al., 2021, ApJS, 253, 3

Hinton S. R., Davis T. M., Lidman C., Glazebrook K., Lewis G. F., 2016, Astron. Comput., 15, 61

Hook I. M., Jørgensen I., Allington-Smith J. R., Davies R. L., Metcalfe N., Murowinski R. G., Crampton D., 2004, PASP, 116, 425

Horne K., 1986, PASP, 98, 609,

Hsiao T. Y.-Y. et al., 2023, preprint (arXiv:2305.03042),

Hunter J. D., 2007, Comput. Sci. Eng., 9, 90

Ishigaki M., Kawamata R., Ouchi M., Oguri M., Shimasaku K., Ono Y., 2018, ApJ, 854, 73

Jakobsen P. et al., 2022, A&A, 661, A80

Jauzac M. et al., 2012, MNRAS, 426, 3369

Jauzac M. et al., 2014, MNRAS, 443, 1549

Jauzac M. et al., 2016, MNRAS, 457, 2029

Jauzac M. et al., 2018, MNRAS, 481, 2901

Johnson T. L., Sharon K., 2016, ApJ, 832, 82

Jullo E., Kneib J.-P., 2009, MNRAS, 395, 1319

Jullo E., Kneib J.-P., Limousin M., Elíasdóttir Á., Marshall P. J., Verdugo T., 2007, New J. Phys., 9, 447

Kartaltepe J. S., Ebeling H., Ma C. J., Donovan D., 2008, MNRAS, 389, 1240

Kassiola A., Kovner I., 1993, ApJ, 417, 450

Keeton C. R., 2001, preprint(astro–ph/0102341)

Keeton C. R., 2010, Gen. Relativ. Gravit., 42, 2151

Kelly P. L. et al., 2018, Nat. Astron., 2, 334

Kikuchihara S. et al., 2020, ApJ, 893, 60

Klypin A. A., Shandarin S. F., 1983, MNRAS, 204, 891

Kneib J.-P., Ellis R. S., Smail I., Couch W. J., Sharples R. M., 1996, ApJ, 471, 643

Kohno K. et al., 2023, preprint (arXiv:2305.15126),

Labbe I. et al., 2023, preprint (arXiv:2306.07320),

Labrie K., Simpson C., Anderson K., Cardenas R., Turner J., Quint B., Conseil S., Oberdorf O., 2021, DRAGONS, Zenodo, Available at: https://doi.org/10.5281/zenodo.5777701

Lagattuta D. J. et al., 2023, MNRAS, 522, 1091

Laporte N. et al., 2021, MNRAS, 505, 4838

Limousin M. et al., 2008, A&A, 489, 23

Lin J., Wagner J., Griffiths R. E., 2023, MNRAS, 526, 2776

Livermore R. C., Finkelstein S. L., Lotz J. M., 2017, ApJ, 835, 113
Mahler G. et al., 2018, MNRAS, 473, 663
Maizy A., Richard J., de Leo M. A., Pelló R., Kneib J. P., 2010, A&A, 509, A105
Mallaby-Kay M. et al., 2021, ApJS, 255, 11
Masters D., Capak P., 2011, PASP, 123, 638
Matthee J. et al., 2024, ApJ, 963, 129
McElwain M. W. et al., 2023, PASP, 135, 058001
Medezinski E., Umetsu K., Okabe N., Nonino M., Molnar S., Massey R., Dupke R., Merten J., 2016, ApJ, 817, 24
Meena A. K., Bagla J. S., 2020, MNRAS, 492, 3294
Meena A. K., Bagla J. S., 2023, MNRAS, 526, 3902
Meena A. K. et al., 2023, ApJ, 944, L6
Menanteau F. et al., 2012, ApJ, 748, 7
Meneghetti M., Bartelmann M., Moscardini L., 2003, MNRAS, 340, 105
Meneghetti M., Bartelmann M., Jenkins A., Frenk C., 2007a, MNRAS, 381, 171
Meneghetti M., Argazzi R., Pace F., Moscardini L., Dolag K., Bartelmann M., Li G., Oguri M., 2007b, A&A, 461, 25
Merten J. et al., 2011, MNRAS, 417, 333
Merten J. et al., 2015, ApJ, 806, 4
Miller T. B. et al., 2018, Nature, 556, 469
Molnar S. M., Broadhurst T., 2015, ApJ, 800, 37
Monna A. et al., 2014, MNRAS, 438, 1417
Monna A. et al., 2015, MNRAS, 447, 1224
Monna A. et al., 2017, MNRAS, 466, 4094
Mullis C. R., Rosati P., Lamer G., Böhringer H., Schwope A., Schuecker P., Fassbender R., 2005, ApJ, 623, L85
Naess S. et al., 2020, J. Cosmol. Astropart. Phys., 2020, 046
Oguri M., 2010, PASJ, 62, 1017
Oguri M., Takada M., Okabe N., Smith G. P., 2010, MNRAS, 405, 2215
Oke J. B., Gunn J. E., 1983, ApJ, 266, 713
Pascale M. et al., 2022a, ApJ, 932, 85
Pascale M. et al., 2022b, ApJ, 938, L6
Pascale M. et al., 2024, preprint (arXiv:2403.18902),
Piqueras L., Conseil S., Shepherd M., Bacon R., Leclercq F., Richard J., 2019, in Molinaro M., Shortridge K., Pasian F.eds, ASP Conf. Ser. Vol. 521, Astronomical Data Analysis Software and Systems XXVI. Astron. Soc. Pac., San Francisco, p. 545
Planck Collaboration XXVII, 2016, A&A, 594, A27
Planck Collaboration IV, 2020, A&A, 641, A4
Price-Whelan A. M. et al., 2018, AJ, 156, 123
Redlich M., Bartelmann M., Waizmann J. C., Fedeli C., 2012, A&A, 547, A66
Repp A., Ebeling H., 2018, MNRAS, 479, 844
Richard J. et al., 2021, A&A, 646, A83
Rieke M. J. et al., 2023, PASP, 135, 028001
Roberts-Borsani G. et al., 2023, Nature, 618, 480
Salmon B. et al., 2020, ApJ, 889, 189
Schechter P., 1976, ApJ, 203, 297
Schlafly E. F., Finkbeiner D. P., 2011, ApJ, 737, 103
Sharon K., Gladders M. D., Rigby J. R., Wuyts E., Koester B. P., Bayliss M. B., Barrientos L. F., 2012, ApJ, 746, 161
Soto K. T., Lilly S. J., Bacon R., Richard J., Conseil S., 2016, MNRAS, 458, 3210
Springel V. et al., 2005, Nature, 435, 629
Strait V. et al., 2020, ApJ, 888, 124
Strait V. et al., 2021, ApJ, 910, 135

Strüder L. et al., 2001, A&A, 365, L18
Sunyaev R. A., Zeldovich Y. B., 1972, Comments Astrophys. Space Phys., 4, 173
Torri E., Meneghetti M., Bartelmann M., Moscardini L., Rasia E., Tormen G., 2004, MNRAS, 349, 476
Turner M. J. L. et al., 2001, A&A, 365, L27
van der Walt S., Colbert S. C., Varoquaux G., 2011, Comput. Sci. Eng., 13, 22
Virtanen P. et al., 2020, Nat. Methods, 17, 261
Wagner J., 2022, A&A, 663, A157,
Weilbacher P. M. et al., 2020, A&A, 641, A28
Welch B. et al., 2022a, Nature, 603, 815
Welch B. et al., 2022b, ApJ, 940, L1
Williams H. et al., 2023, Science, 380, 416
Wright E. L. et al., 2010, AJ, 140, 1868
Zeldovich I. B., Einasto J., Shandarin S. F., 1982, Nature, 300, 407
Zitrin A., Broadhurst T., Rephaeli Y., Sadeh S., 2009, ApJ, 707, L102
Zitrin A. et al., 2013a, ApJ, 762, L30
Zitrin A., Menanteau F., Hughes J. P., Coe D., Barrientos L. F., Infante L., Mandelbaum R., 2013b, ApJ, 770, L15
Zitrin A. et al., 2015, ApJ, 801, 44
Zitrin A. et al., 2017, ApJ, 839, L11

SUPPORTING INFORMATION

Supplementary data are available at *MNRAS* online.

MACS0600_Furtak+24_cluster-members.fits
MACS0600_Furtak+24_multiple-images.fits
v2.0_Fig-1_high-resolution.pdf
v2.0_Fig-5_high-resolution.pdf
v2.0_Fig-8_high-resolution.pdf

Please note: Oxford University Press is not responsible for the content or functionality of any supporting materials supplied by the authors. Any queries (other than missing material) should be directed to the corresponding author for the article.

APPENDIX A: MULTIPLE-IMAGE TABLE

The multiple images and candidates identified in MACS0600 are all listed in Table A1, and shown in Fig. 5. The spectroscopic redshift measurement of system 7 comes from the ALMA data and was first published in Fujimoto et al. (2021). Other spectroscopic redshifts were measured with MUSE as described in Section 2.4 (for the method, see also Richard et al. 2021). Most of the MUSE multiple image spectroscopic redshifts are based on the Lyman α line, apart for systems 1, 2, 3, 10, 18, and 19 which are based on absorption lines and forbidden emission lines. All MUSE spectroscopic redshifts shown in Table A1 have confidence levels of 2 or 3. A machine-readable version of Table A1 is available in the online supplementary material of this paper and contains further information: cross-matching to the public RELICS catalogue and the MUSE catalogue that will be made publicly available on the Richard et al. (2021) Atlas of MUSE observations towards massive lensing clusters website, and flagging if used in our model or not.

Table A1. Multiple images and candidates identified in the Anglerfish cluster.

ID	RA	Dec.	z_{spec}	z_{phot} [95 per cent-range]	z_{model} [95 per cent-range]	Remarks
1.1	06:00:10.038	−20:07:45.283	2.0032 ± 0.0001	–	–	
1.2	06:00:09.619	−20:07:40.883	2.0033 ± 0.0002	–	–	
1.3	06:00:08.341	−20:07:31.183	–	–	–	
2.1	06:00:08.422	−20:08:37.754	2.7699 ± 0.0002	–	–	
2.2	06:00:08.182	−20:08:37.379	2.7734 ± 0.0002	–	–	
3.1	06:00:08.567	−20:08:37.879	2.7699 ± 0.0002	–	–	
3.2	06:00:08.105	−20:08:37.129	2.7734 ± 0.0002	–	–	
4.1	06:00:09.957	−20:07:26.558	–	–	4.61 [4.59,4.63]	
4.2	06:00:10.230	−20:07:29.278	–	4.8 [4.7,5.0]	’’	
5.1	06:00:10.906	−20:07:24.800	–	1.7 [1.6,1.8]	1.84 [1.77,1.87]	
5.2	06:00:09.978	−20:07:00.900	–	–	’’	Close to West BCG.
5.3	06:00:10.199	−20:07:01.100	–	–	’’	’’
5.4	06:00:10.349	−20:06:59.300	–	1.1 [1.0,1.2]	’’	’’
5.5	06:00:09.734	−20:06:46.570	–	0.2 [0.1,2.2]	’’	
6.1	06:00:11.200	−20:07:19.700	–	1.6 [1.3,1.7]	1.66 [1.63,1.69]	Tentative $z_{spec} \simeq 1.5774$ from GMOS.
6.2	06:00:10.357	−20:06:45.400	–	0.7 [0.1,1.7]	’’	
6.3	06:00:10.646	−20:06:52.900	–	0.6 [0.2,2.3]	’’	
6.4	06:00:10.705	−20:06:50.380	–	–	’’	
7.1	06:00:09.258	−20:08:25.725	6.0719 ± 0.0004	–	–	Multiply-imaged ALMA system
7.2	06:00:09.002	−20:08:27.381	’’	–	–	(Fujimoto et al. 2021; Laporte et al. 2021).
7.3	06:00:08.562	−20:08:12.260	’’	–	–	’’; Analysed in Fujimoto et al. (2024).
7.4	06:00:09.554	−20:08:10.749	’’	–	–	
7.5	06:00:05.305	−20:07:27.646	–	–	–	Counter-image confirmed with *JWST*.
8.1	06:00:08.027	−20:08:24.975	5.4603 ± 0.0001	–	–	
8.2	06:00:10.317	−20:08:12.355	5.4599 ± 0.0001	–	–	
8.3	06:00:10.146	−20:08:01.761	5.4603 ± 0.0001	–	–	
9.1	06:00:10.199	−20:08:11.399	3.521 ± 0.001	–	–	
9.2	06:00:08.103	−20:08:23.457	3.5247 ± 0.0003	–	–	
9.3	06:00:10.073	−20:08:02.763	3.5169 ± 0.0009	–	–	
9.4	06:00:08.235	−20:08:11.677	3.5228 ± 0.0003	–	–	
10.1	06:00:08.616	−20:08:13.016	4.5064 ± 0.0001	–	–	
10.2	06:00:09.470	−20:08:14.156	4.5066 ± 0.0001	–	–	
10.3	06:00:09.160	−20:08:24.086	4.5071 ± 0.0002	–	–	
11.1	06:00:10.312	−20:08:09.741	3.6753 ± 0.0001	–	–	
11.2	06:00:10.212	−20:08:02.284	3.6753 ± 0.0001	–	–	
12.1	06:00:10.224	−20:07:49.108	5.1734 ± 0.0001	–	–	
12.2	06:00:10.928	−20:08:06.870	5.1739 ± 0.0002	–	–	
13.1	06:00:10.470	−20:08:32.123	3.0292 ± 0.0002	–	–	
13.2	06:00:08.533	−20:07:48.574	3.0292 ± 0.0003	–	–	
14.1	06:00:09.807	−20:08:35.307	4.4406 ± 0.0003	–	–	
14.2	06:00:08.977	−20:07:56.741	4.4404 ± 0.0002	–	–	
15.1	06:00:07.319	−20:08:05.092	3.9478 ± 0.0006	–	–	
15.2	06:00:07.491	−20:08:04.934	3.947 ± 0.003	–	–	
15.3	06:00:11.100	−20:08:34.476	3.945 ± 0.004	–	–	
16.1	06:00:09.037	−20:08:05.542	4.1399 ± 0.0008	–	–	Radial system; close to south BCG.
16.2	06:00:08.604	−20:08:08.207	4.1326 ± 0.0002	–	–	’’
17.1	06:00:09.727	−20:07:57.920	3.32 ± 0.05	–	–	
17.2	06:00:10.296	−20:08:19.373	3.3162 ± 0.0001	–	–	
17.3	06:00:07.755	−20:08:23.942	3.3162 ± 0.0001	–	–	
18.1	06:00:08.078	−20:08:20.160	3.6672 ± 0.0003	–	–	
18.2	06:00:10.312	−20:08:09.741	3.674 ± 0.001	–	–	
19.1	06:00:07.901	−20:07:49.735	3.9500 ± 0.0004	–	–	
19.2	06:00:07.877	−20:08:04.171	3.9370 ± 0.0002	–	–	
20.1	06:00:07.966	−20:07:52.637	5.3550 ± 0.0001	–	–	

Table A1 – *continued*

ID	RA	Dec.	z_{spec}	z_{phot} [95 per cent-range]	z_{model} [95 per cent-range]	Remarks
20.2	06:00:10.913	−20:08:39.110	5.3549 ± 0.0006	–	–	
21.1	06:00:06.799	−20:08:15.872	–	–	–	
21.2	06:00:08.583	−20:07:46.257	5.4086 ± 0.0002	–	–	
21.3	06:00:10.745	−20:08:33.675	5.4087 ± 0.0001	–	–	
22.1	06:00:08.994	−20:07:45.452	3.526 ± 0.001	–	–	
22.2	06:00:10.718	−20:08:24.385	3.529 ± 0.004	–	–	
22.3	06:00:07.392	−20:08:18.134	3.529 ± 0.001	–	–	
23.1	06:00:07.477	−20:07:39.701	5.4087 ± 0.0002	–	–	
23.2	06:00:07.709	−20:07:40.085	5.4090 ± 0.0003	–	–	
c24.1	06:00:20.084	−20:06:40.052	–	–	2.62 [2.55,2.70]	System identified in the GMOS imaging.
c24.2	06:00:20.076	−20:06:41.400	–	–	,,	,,
c24.3	06:00:19.472	−20:07:40.794	–	–	,,	,,
c25.1	06:00:20.667	−20:06:58.993	–	–	–	Close to BCG1; possible giant arc.
c25.2	06:00:20.673	−20:07:01.917	–	–	–	,,; System identified in the GMOS imaging.
c25.3	06:00:17.208	−20:06:10.908	–	–	–	
26.1	06:00:05.591	−20:08:54.752	–	1.8 [1.2,2.0]	2.14 [1.99,2.45]	Galaxy–galaxy system.
26.2	06:00:05.303	−20:08:51.220	–	1.1 [0.7,1.6]	,,	
26.3	06:00:05.398	−20:08:53.966	–	–	,,	
26.4	06:00:05.453	−20:08:52.327	–	1.0 [0.9,1.1]	,,	
27.1	06:00:07.351	−20:08:07.433	–	–	7.01 [6.70,7.25]	System identified in *JWST* imaging.
27.2	06:00:07.591	−20:08:06.868	–	–	,,	,,
28.1	06:00:08.897	−20:08:06.337	–	–	2.76 [2.72,2.92]	Radial system; close to south BCG.
28.2	06:00:08.817	−20:08:08.057	–	1.8 [1.4,2.5]	,,	,,
c29.1	06:00:08.917	−20:08:08.118	–	–	–	Radial system; close to south BCG.
c29.2	06:00:08.531	−20:08:09.482	–	–	–	,,
30.1	06:00:05.602	−20:08:35.526	–	–	6.69 [6.26,7.10]	System identified in *JWST* imaging.
30.2	06:00:05.744	−20:08:38.406	–	–	,,	,,
c31.1	06:00:14.186	−20:07:29.545	–	0.5 [0.2,2.5]	1.06 [1.05,1.10]	
c31.2	06:00:14.159	−20:07:27.857	–	2.5 [1.4,2.8]	,,	
c32.1	06:00:13.784	−20:07:29.722	–	–	3.78 [3.76,3.80]	
c32.2	06:00:13.737	−20:07:27.920	–	–	,,	
c33.1	06:00:16.581	−20:06:38.658	–	–	1.05 [1.03,1.06]	System identified in the GMOS imaging.
c33.2	06:00:16.958	−20:06:46.349	–	–	,,	,,
c33.3	06:00:17.301	−20:07:21.123	–	–	,,	,,
c34.1	06:00:20.142	−20:07:10.303	–	–	–	Faint and diffuse, only detected in the *i* band.
c34.2	06:00:17.046	−20:06:13.842	–	–	–	,,; System identified in the GMOS imaging.
c34.3	06:00:18.269	−20:07:38.249	–	–	–	,,
c35.1	06:00:13.452	−20:07:06.246	–	1.2 [1.1,1.3]	–	At the eastern edge of the *HST* imaging.
c35.2	06:00:20.841	−20:06:50.397	–	–	–	Detected in the GMOS imaging.

Note. Column 1: image ID. *Columns 2 and 3*: right ascension and declination. *Column 4*: spectroscopic redshift. *Column 5*: photometric redshift and its 95 per cent (2σ) range as computed with BPZ in the RELICS catalogue (see Section 2.3). *Column 6*: median redshift from our SL-model (see Section 4.3). *Column 7*: additional remarks.

[1]*Department of Physics, Ben-Gurion University of the Negev, P.O. Box 653, Be'er-Sheva 84105, Israel*

[2]*CNRS, Centre de Recherche Astrophysique de Lyon UMR 5574, Université Lyon 1, ENS de Lyon, F-69230 Saint-Genis Laval, France*

[3]*Department of Astronomy, University of Geneva, Ch. d'Ecogia 16, CH-1290 Versoix, Switzerland*

[4]*California Institute of Technology, 1200 East California Boulevard, Pasadena, CA 91125, USA*

[5]*Institute for Astronomy, University of Hawaii, 640 N. Aohoku Place, Hilo, HI 96720, USA*

[6]*Department of Astronomy, The University of Texas at Austin, Austin, TX 78712, USA*

[7]*Aix Marseille Université, CNRS, CNES, LAM (Laboratoire d'Astrophysique de Marseille), UMR 7326, F-13388 Marseille, France*

[8]*Centre for Extragalactic Astronomy, Durham University, South Road, Durham DH1 3LE, UK*

[9]*Institute for Computational Cosmology, Durham University, South Road, Durham DH1 3LE, UK*

[10]*STAR Institute, Quartier Agora - Allée du six Août, 19c B-4000 Liège, Belgium*

[11]*Department of Liberal Arts and Sciences, Berklee College of Music, 7 Haviland Street, Boston, MA 02215, USA*

[12]*Center for Astrophysics, Harvard & Smithsonian, 60 Garden Street, Cambridge, MA 02138, USA*

[13]*Steward Observatory, University of Arizona, 933 N Cherry Ave, Tucson AZ 85721, USA*

[14]*Astrophysics Research Centre, University of KwaZulu-Natal, Westville Campus, Durban 4041, South Africa*

[15]*School of Mathematics, Statistics & Computer Science, University of KwaZulu-Natal, Westville Campus, Durban 4041, South Africa*

[16]*Space Telescope Science Institute, 3700 San Martin Drive, Baltimore, MD 21218, USA*

[17]*Institute of Astronomy, Graduate School of Science, The University of Tokyo, 2-21-1 Osawa, Mitaka, Tokyo 181-0015, Japan*

[18]*Research Center for the Early Universe, Graduate School of Science, The University of Tokyo, 7-3-1 Hongo, Bunkyo-ku, Tokyo 113-0033, Japan*

[19]*Departamento de Física Teórica y del Cosmos, Campus de Fuentenueva, Edificio Mecenas, Universidad de Granada, E-18071 Granada, Spain*

[20]*Facultad de Ciencias, Instituto Carlos I de Física Teórica y Computacional, E-18071 Granada, Spain*

[21]*LPNHE, CNRS/IN2P3, Sorbonne Université, Université Paris Cité, Laboratoire de Physique Nucléaire et de Hautes Énergies, F-75005 Paris, France*

This paper has been typeset from a TEX/LATEX file prepared by the author.